water

MDPI

*Review*

# Graphitic Carbon Nitride-Based Materials for PMS-Assisted Visible-Light Photocatalytic Degradation of Antibiotics: Synthesis, Mechanisms, and Future Perspectives

**Waqas Umar [1], Fawad Ali [1], Syed Izaz Ali Shah [1], Muhammad Anwar [1], Saeed Ahmad [1], Muhammad Ateeq [1], Noor S. Shah [2], Javed Ali Khan [1,*] and Changseok Han [3,4,*]**

[1] Department of Chemistry, Abdul Wali Khan University Mardan, Mardan 23200, Pakistan
[2] Department of Chemistry, COMSATS University Islamabad, Abbottabad Campus, Abbottabad 22060, Pakistan
[3] Program in Environmental and Polymer Engineering, Graduate School of Inha University, 100 Inha-ro, Michuhol-gu, Incheon 22212, Republic of Korea
[4] Department of Environmental Engineering, Inha University, 100 Inha-ro, Michuhol-gu, Incheon 22212, Republic of Korea
* Correspondence: javedkhan@awkum.edu.pk or khanjaved2381@gmail.com (J.A.K.); hanck@inha.ac.kr (C.H.)

**Abstract**

The rapid increase in antibiotic resistance has driven growing interest in advanced photocatalytic materials for the effective removal of antibiotic pollutants from wastewater systems. Among these materials, graphitic carbon nitride (g-$C_3N_4$), a metal-free polymeric semiconductor, has emerged as a sustainable and efficient photocatalyst due to its strong visible-light activity, excellent chemical stability, and tunable electronic properties. This review presents a comprehensive overview of recent advances in the synthesis of g-$C_3N_4$-based materials for peroxymonosulfate (PMS)-assisted visible-light-driven photocatalytic degradation of antibiotics. The antibiotics discussed in this review include tetracycline, ciprofloxacin, levofloxacin, sulfamethoxazole, sulfamethazine, doxycycline, oxytetracycline, and moxifloxacin, along with other pharmaceutical contaminants. The fundamental degradation mechanisms, including the generation of reactive oxygen species (ROS), PMS activation pathways, and interfacial charge-transfer processes, are systematically discussed. Furthermore, this review addresses factors influencing photocatalytic performance, including photocatalyst dosage, solution pH, temperature, pollutant concentration, and light intensity. Finally, the current challenges and future perspectives for the practical application of g-$C_3N_4$-based materials in wastewater treatment are highlighted.

**Keywords:** g-$C_3N_4$-based materials; PMS activation; photocatalysis; antibiotics; degradation; wastewater treatment

Check for updates

Academic Editors: Laura Scrano and Monica Brienza

Received: 15 June 2026
Revised: 19 July 2026
Accepted: 21 July 2026
Published: 4 August 2026

**Copyright:** © 2026 by the authors. Licensee MDPI, Basel, Switzerland. This article is an open access article distributed under the terms and conditions of the Creative Commons Attribution (CC BY) license.

## 1. Introduction

Water is an essential natural resource that plays a vital role in sustaining life and maintaining environmental balance on Earth [1]. Approximately 71% of the Earth's surface is covered by water, including oceans, glaciers, rivers, lakes, and other water bodies. However, more than 96.5% of this water is saline, while only 2.5% is freshwater. Of this freshwater, nearly 1.9% is stored in glaciers and ice caps, leaving only a small fraction readily available for human use [2,3]. Rapid population growth, urbanization, and industrialization have intensified environmental pollution, particularly water contamination [4]. Water pollution

is defined as the introduction of contaminants into water bodies beyond permissible limits [5]. Major water pollutants include dyes, heavy metals, aliphatic and aromatic organic compounds, pharmaceutical residues, agricultural wastes (i.e., pesticides and fertilizers), and pathogenic microorganisms [6,7]. The continuous release of these pollutants into rivers, ponds, seas, and oceans has significantly reduced the availability of safe drinking water. According to the World Health Organization (WHO), nearly 2.5 billion people lack access to clean drinking water [8]. In addition, about 380 billion $m^3$ of domestic and urban wastewater is generated worldwide each year, and this volume is projected to increase by nearly 51% by 2050, posing a serious challenge to global water resource management [9].

Among emerging contaminants, pharmaceuticals have attracted significant global attention due to their widespread occurrence and persistence in aquatic environments [10]. Pharmaceuticals are biologically active compounds widely used for the treatment and prevention of diseases; however, their continuous release into the environment has raised serious concerns regarding ecological and human health risks [11]. Due to incomplete metabolism in the human body, a large fraction of pharmaceuticals is excreted unchanged or as metabolites and enters wastewater systems through domestic discharge, hospital effluents, and improper disposal [12,13]. Recently, about 3,000 pharmaceutical compounds have been detected in water bodies [14], with reported concentrations ranging from ng $L^{-1}$ to several hundred μg $L^{-1}$ across different regions and aquatic environments [15]. For example, naproxen, ketoprofen, diclofenac and ibuprofen have been detected at concentrations of 551,960, 233,630, 40,570, and 31,250 ng $L^{-1}$, respectively, in Poland [16]. Similarly, carbamazepine (CBZ) has been reported in groundwater, drinking water, rivers, and wastewater treatment effluents in Germany at concentrations of 610 ng $L^{-1}$, 18 ng $L^{-1}$, 0.25 μg $L^{-1}$, and 2.1 μg $L^{-1}$, respectively [12]. The presence of such pharmaceuticals in aquatic environments may lead to chronic diseases, allergic reactions, and other adverse effects on human health [17]. Moreover, several toxicological studies have reported that acetaminophen exhibited genotoxic and hepatotoxic effects and inhibited the reproduction of *Daphnia magna* [18], while propranolol showed cytotoxic effects against *Vibrio fischeri* [19].

Among various pharmaceuticals, antibiotics are antimicrobial agents used to inhibit or eliminate bacterial pathogens for the treatment and prevention of infectious diseases. Similar to other pharmaceuticals, a significant fraction (30–90%) of administered antibiotics is excreted unchanged and subsequently released into the environment through domestic wastewater, hospital discharges, and agricultural runoff [20,21]. As a result, antibiotic residues are frequently detected in diverse aquatic systems. For instance, ciprofloxacin (CIP) has been detected at concentrations of 11–99 μg $L^{-1}$ and 0.032 μg $L^{-1}$ in wastewater and drinking water samples, respectively [22]. Sulfamethoxazole (SMX) has been found at concentrations of up to 54.83 mg $L^{-1}$ in livestock wastewater discharges [23]. Other antibiotics, including trimethoprim, tetracycline, and clindamycin, have been detected in wastewater treatment plant (WWTP) effluents at concentrations ranging from 0.090 to 6.0 μg $L^{-1}$ [24]. In addition, ofloxacin was detected at concentrations above 13 μg $L^{-1}$ in hospital wastewater in Spain [25]. The prolonged presence of antibiotics in natural environments poses a serious risk to human health and the environment, particularly due to the development and spread of antibiotic resistance genes (ARGs) and antibiotic-resistant bacteria (ARBs) [26]. Various toxic effects of antibiotics on plants, algae, and aquatic organisms have been reported in the literature. For example, quinolone antibiotics have been reported to inhibit the growth and development of rice seedlings [27]. Fluoroquinolone antibiotics, including enrofloxacin, flumequine, and levofloxacin, were found to cause embryotoxicity and delayed acute toxicity in *Daphnia magna* during neonatal exposure [28]. Erythromycin exhibited significant toxicity toward the antioxidant system of *P. subcapitata* by reducing ascorbic acid and glutathione levels and inducing oxidative stress [29]. Moreover, ofloxacin

adversely affected the growth and photosynthesis of tomatoes and Welsh onions [27]. Due to the rapid increase in antimicrobial resistance, drug-resistant infections currently account for approximately 700,000 deaths annually worldwide, and this number is expected to reach 10 million deaths per year by 2050 [30]. Therefore, the effective removal of antibiotics from water has become an urgent environmental and public health necessity.

Various technologies, including ion exchange [31], disinfection [32], biodegradation, adsorption, membrane separation, and coagulation, have been investigated for the removal of antibiotics from water bodies [26]. However, the practical application of these techniques is limited due to their high operational costs and incomplete degradation of pollutants. On the other hand, advanced oxidation processes (AOPs) are considered among the most promising technologies for the degradation of antibiotics, as they can transform these contaminants into low-molecular-weight compounds, thereby reducing antimicrobial effects and enhancing biodegradability and overall removal efficiency [33]. Different types of AOPs have been developed, such as UV-based processes (e.g., UV/$H_2O_2$ and UV/$TiO_2$), photocatalysis, ozone-based processes, Fenton and photo-Fenton processes, and sonolysis [34,35].

Among various AOPs, photocatalysis has been recognized as a cost-effective, efficient, and eco-friendly technology for pollutant degradation. To further improve its degradation efficiency, various oxidizing agents, including hydrogen peroxide ($H_2O_2$), persulfate (PS), ozone ($O_3$), and peroxymonosulfate (PMS), have been incorporated into photocatalytic systems. $H_2O_2$ is commonly used because of its low cost and ability to produce hydroxyl radicals ($^{\bullet}OH$); however, its activation efficiency under visible-light irradiation is relatively limited, and it may undergo self-decomposition. PS exhibits high chemical stability but generally requires higher activation energy than PMS due to the cleavage of its symmetric peroxide bond. $O_3$ possesses strong oxidative capability; however, its low water solubility and high operational cost limit its practical application. Among these oxidizing agents, PMS has attracted significant attention due to its high oxidation potential, broad operational pH range, and ease of activation under visible-light irradiation. Moreover, its excellent compatibility with g-$C_3N_4$-based photocatalysts promotes efficient charge separation and enhances photocatalytic degradation performance [36,37].

Upon light irradiation, semiconductor photocatalysts absorb photons with energies equal to or greater than their bandgap, promoting electrons from the valence band (VB) to the conduction band (CB) and generating electron–hole ($e^-$–$h^+$) pairs. These photogenerated charge carriers, particularly electrons, activate PMS, leading to the generation of ROS, including hydroxyl radicals ($^{\bullet}OH$), sulfate radicals ($SO_4^{\bullet-}$), and superoxide radical anions ($O_2^{\bullet-}$) [38]. These reactive species play a crucial role in the degradation and complete mineralization of target pollutants into $CO_2$, $H_2O$, and other harmless products. A variety of semiconductor photocatalysts, such as zinc sulfide (ZnS), vanadium pentoxide ($V_2O_5$), titanium dioxide ($TiO_2$), and cerium oxide ($CeO_2$), have been employed for the removal of antibiotics from aquatic systems [39,40]. Nevertheless, these photocatalysts are associated with some limitations, such as wide bandgaps, limited visible-light responsiveness, photocorrosion, and a rapid recombination rate of photoinduced charge carriers, which significantly reduces their photocatalytic performance [41]. For example, ZnO and $TiO_2$ are primarily active under UV irradiation due to their wide bandgaps of approximately 3.37 and 3.2 eV, respectively [42,43].

Among metal-free semiconductor, g-$C_3N_4$ has gained widespread attention as a promising photocatalyst for antibiotic degradation. This is due to its unique properties, including non-toxicity, suitable electronic band alignment, high thermal and chemical stability, and low-cost synthesis [44]. g-$C_3N_4$ exhibits a moderate bandgap of about 2.7 eV, with suitable conduction band (CB) and valence band (VB) edge positions of –1.3 and 1.4 eV,

respectively, thereby enabling efficient utilization of visible light [45,46]. In addition, g-$C_3N_4$ is composed of earth-abundant elements (carbon and nitrogen), thereby lowering the synthesis costs and providing excellent physicochemical stability [47]. However, pristine g-$C_3N_4$ suffers from various limitations, such as rapid recombination of photogenerated electron–hole pairs, limited light utilization, and low surface area, which significantly hinder its photocatalytic activity [48]. To overcome these limitations, various enhancement strategies have been developed, including non-metal and metal doping, nanostructure fabrication, semiconductor coupling, and heterojunction formation [49,50]. For example, the deposition of noble metals such as Au, Ru, and Pt is an effective method for enhancing the photocatalytic performance of g-$C_3N_4$ due to their superior conductivity and light absorption capabilities [51]. Furthermore, heterojunction engineering, including Z-scheme, S-scheme, and type-II heterojunctions, significantly facilitates charge carrier separation and improves overall photocatalytic efficiency [52]. Recent studies have further shown that heterostructure engineering is an effective strategy for improving the photocatalytic degradation of emerging contaminants by enhancing light absorption, charge separation, and reactive species generation. In addition, organic semiconductors such as g-$C_3N_4$ have attracted increasing attention in photocatalysis because of their metal-free nature, visible-light response, tunable electronic structure, and potential applications in organic transformations and environmental remediation [53,54].

Several recent review articles have discussed the application of g-$C_3N_4$-based photocatalysts for environmental remediation from different perspectives. For example, Khan et al. [55] comprehensively reviewed the synthesis, doping strategies, photocatalytic mechanisms, and environmental applications of doped g-$C_3N_4$. Bineta et al. [56] summarized the recent advances in g-$C_3N_4$-based photocatalysts for antibiotic photodegradation, focusing primarily on catalyst modification strategies and the factors affecting photocatalytic performance. Likewise, Imran et al. [57] reviewed g-$C_3N_4$/metal oxide nanocomposites for antibiotic degradation, with particular emphasis on heterojunction construction and charge transfer mechanisms. Although these reviews provide valuable insights into the design and application of g-$C_3N_4$-based photocatalysts, a comprehensive discussion integrating PMS-assisted visible-light photocatalysis with antibiotic degradation remains limited. In particular, the relationships among catalyst design, PMS activation pathways, reactive oxygen species (ROS) generation, and the operational factors governing degradation efficiency have not been systematically discussed in a single review.

This review presents a comprehensive overview of g-$C_3N_4$-based photocatalytic systems for the removal of antibiotics from wastewater, with particular emphasis on PMS-assisted visible-light photocatalysis. It focuses on recent advances in synthesis strategies, modified g-$C_3N_4$ nanocomposites, and their role in enhancing photocatalytic performance. Special emphasis is given to degradation mechanisms, particularly PMS activation pathways and ROS generation. Furthermore, the review highlights the influence of key operational parameters such as catalyst dosage, pH, pollutant concentration, and light intensity on photocatalytic efficiency. Finally, this review aims to offer strategic guidance for the rational design of g-$C_3N_4$-based photocatalytic and PMS-activated systems to support sustainable environmental remediation.

## 2. Synthesis Methods

A wide range of methods have been developed for the fabrication of g-$C_3N_4$-based materials. This review mainly discusses the most commonly used synthesis methods for g-$C_3N_4$-based materials, including hydrothermal, solvothermal, microwave-assisted, calcination, and green synthesis methods. These methods are discussed in detail in the following sections.

### *2.1. Synthesis of Pristine g-$C_3N_4$*

Pure g-$C_3N_4$ is commonly synthesized via calcination of nitrogen-rich precursors, including urea, melamine, dicyandiamide, and cyanamide at elevated temperatures. Among these precursors, melamine is the most widely used due to its high nitrogen content, low cost, and structural similarity to the heptazine units present in g-$C_3N_4$. Typically, the precursors are calcined in a muffle furnace at temperatures ranging from 500 to 600 °C, leading to polycondensation and the formation of layered g-$C_3N_4$ structures. The synthesized pristine g-$C_3N_4$ exhibits a two-dimensional layered morphology, a moderate surface area, and a bandgap of approximately 2.7 eV, enabling visible-light-driven photocatalytic activity. Furthermore, synthesis parameters such as precursor type, calcination temperature, and heating rate significantly affect the photocatalytic, optical, and structural properties of the resulting g-$C_3N_4$ nanomaterials [58,59].

### *2.2. Synthesis Methods of g-$C_3N_4$-Based Materials*

#### 2.2.1. Hydrothermal/Solvothermal Process

The hydrothermal process refers to chemical reactions carried out in water under high temperature and high pressure in a sealed reaction vessel [60]. In contrast, the solvothermal process employs organic or non-aqueous solvents instead of water [61]. Typically, hydrothermal synthesis is carried out in a stainless-steel Teflon-lined autoclave under well-controlled conditions, usually at temperatures below 200 °C and pressures under 10 MPa in aqueous solution. This process occurs through several stages, including crystal growth, phase transformation, and phase equilibrium, which together facilitate the formation of fine or ultrafine crystalline materials [60].

Hydrothermal and solvothermal methods are commonly used for the preparation of advanced functional materials. By optimizing reaction parameters such as temperature, pressure, reaction time, and solvent type, these approaches enable precise control over the morphology and photocatalytic performance [62]. Therefore, these methods have been extensively employed for the preparation and modification of g-$C_3N_4$-based materials. For example, Vijayakumar et al. [63] synthesized a CuO/g-$C_3N_4$ heterostructure via a hydrothermal approach using copper nitrate [$Cu(NO_3)_2$] as the copper precursor. The reaction pH was adjusted to 13 using NaOH. The bandgaps of pristine CuO, g-$C_3N_4$, and the CuO/g-$C_3N_4$ heterostructure were found to be 1.40, 2.70, and 1.30 eV, respectively. The as-prepared CuO/g-$C_3N_4$ composite forms a hybrid VB/CB alignment, which effectively suppresses the recombination of photogenerated $e^-$–$h^+$ pairs, thereby significantly enhancing its photocatalytic degradation performance compared with pristine CuO and g-$C_3N_4$ components. Similarly, Hao et al. [64] prepared a g-$C_3N_4$/$TiO_2$ heterojunction using an in situ hydrothermal approach followed by calcination. Melamine and titanium tetrachloride ($TiCl_4$) were used as precursors. The g-$C_3N_4$/$TiO_2$ composites were synthesized using different amounts of melamine (0.5, 1, 2, 3, and 4 g), and the resulting composites were named TC0.5, TC1, TC2, TC3, and TC4, respectively. Their corresponding specific surface areas were 32.1, 45, 87.2, 115.6, and 58.3 $m^2\ g^{-1}$, respectively. Among all the samples, TC3 demonstrated the highest photocatalytic performance, achieving 95.2% degradation of Rhodamine B under optimized reaction conditions. Furthermore, Wang et al. [65] fabricated g-$C_3N_4$/carbon quantum dot (CQD) composites via a solvothermal method. g-$C_3N_4$ nanosheets and CQDs were separately synthesized using melamine and citric acid as precursors, respectively. The resulting composites were prepared by mixing g-$C_3N_4$ with different volumes (5, 10, 20, 40, and 60 mL) of CQD solution and were labeled CN-5 to CN-60. TEM analysis revealed that CQDs with an average particle size of about 8 nm were uniformly dispersed on the surface of g-$C_3N_4$ nanosheets, indicating strong interfacial interactions. CN-20 showed the highest photocatalytic activity, with a kinetic rate constant

of 0.0219 $min^{-1}$, corresponding to a fourfold enhancement over pristine g-$C_3N_4$. Shanaah et al. [66] synthesized Co@g-$C_3N_4$ nanorods via a controlled hydrothermal approach. First, g-$C_3N_4$ was synthesized by the calcination of urea, followed by $HNO_3$ treatment to obtain layered nanosheets with higher surface area and larger pore volume. Subsequently, 1 g of the as-prepared g-$C_3N_4$ and 1 g of cobalt(II) nitrate hexahydrate [$Co(NO_3)_2.6H_2O$] were dispersed in distilled water, followed by sonication and hydrothermal treatment at 160 °C for 16 h. The resulting product was washed with distilled water, filtered, and dried to obtain the final Co@g-$C_3N_4$ nanorods. The overall synthesis procedure is illustrated in Figure 1a. Moreover, cobalt doping markedly reduces the bandgap of g-$C_3N_4$ from 2.92 eV to 0.54 eV, thereby facilitating rapid electron transfer and enhancing electrical conductivity.

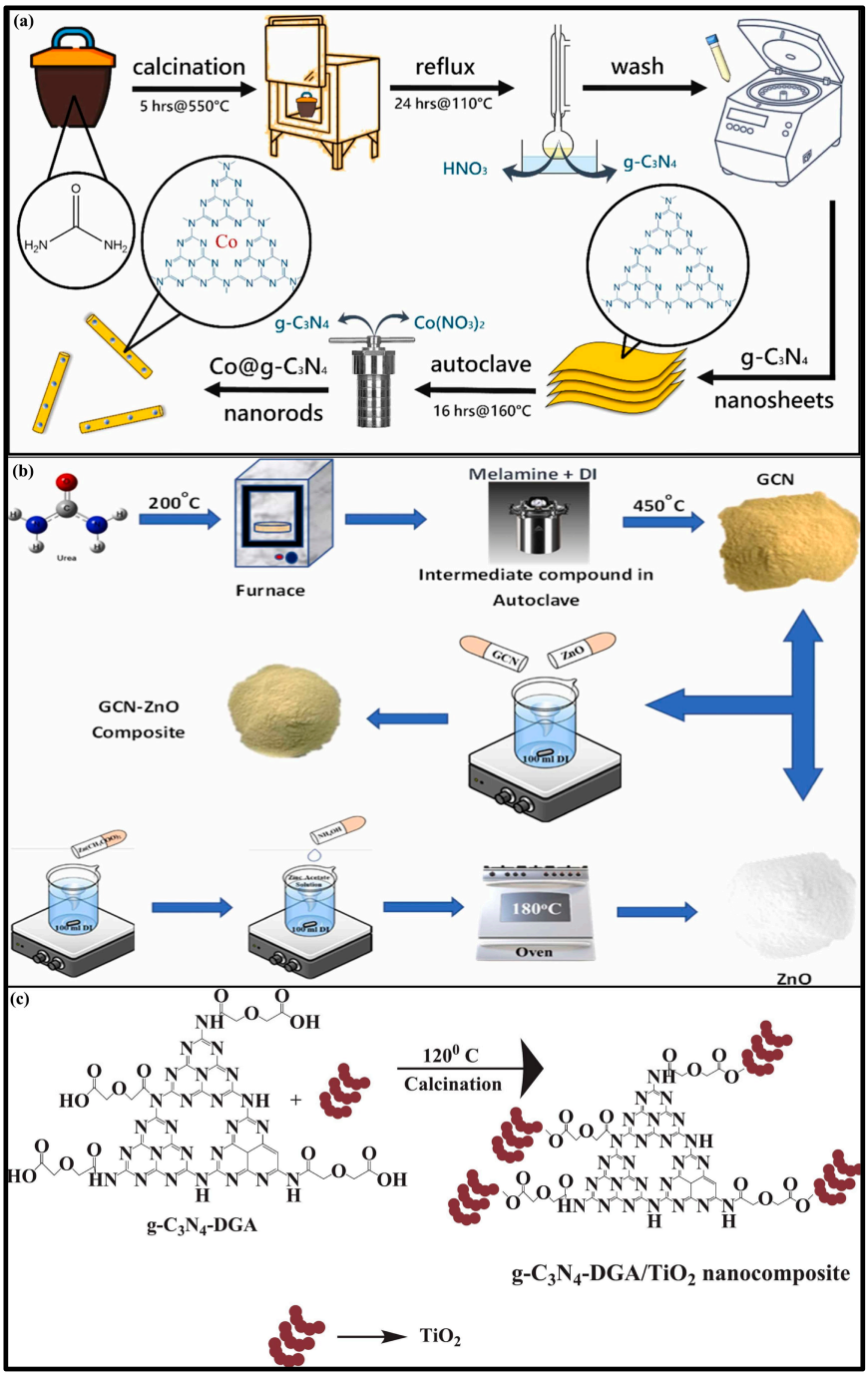



**Figure 1.** (**a**) Schematic illustration of the experimental procedure. Adapted from [66], which is open access and permits unrestricted use of the material under the terms of the creative commons CC-BY,

(**b**) Schematic representation of the synthesis of g-$C_3N_4$ and Co@g-$C_3N_4$. Adapted from [67], which is open access and permits unrestricted use of materials under the terms of the creative commons CC-BY. (**c**) Schematic illustration of the synthesis of $TiO_2$@g-$C_3N_4$-HDGA nanocomposite. Adapted from [68], which is open access and permits unrestricted use of the material under the terms of the creative commons CC-BY.

Kumar et al. [67] synthesized a graphitic carbon nitride/zinc oxide (GCN-ZnO) hybrid using a combination of wet-chemical and hydrothermal methods. First, g-$C_3N_4$ was synthesized via calcination, whereas ZnO was prepared using a wet-chemical approach. The as-prepared g-$C_3N_4$ and ZnO were uniformly dispersed in deionized water, followed by thermal treatment at 120 °C for 3 h to obtain the GCN-ZnO hybrid (Figure 1b). The resulting hybrid consisted of crystalline ZnO microrods anchored on an amorphous g-$C_3N_4$ matrix through van der Waals interactions. These interactions effectively suppressed oxygen-related defects in ZnO, leading to enhanced blue–cyan emission and improved optoelectronic properties. Dhanu et al. [68] synthesized a $TiO_2$@g-$C_3N_4$-HDGA nanocomposite via a solvothermal method. In this approach, the pre-synthesized anatase $TiO_2$ nanoparticles and HDGA-functionalized g-$C_3N_4$ were uniformly dispersed in deionized water, followed by sonication and thermal treatment at 120 °C for 12 h to achieve intimate interfacial integration (Figure 1c). The as-prepared nanocomposite exhibited a specific surface area, pore volume, and pore diameter of 253.812 $m^2\ g^{-1}$, 0.929 $cm^3\ g^{-1}$, and 423 nm, respectively.

#### 2.2.2. Microwave-Assisted Method

Microwave-assisted synthesis has attracted significant interest as a cost-effective, sustainable, and efficient method for the preparation of advanced materials [69]. In this approach, microwave radiation interacts directly with the reaction medium, enabling rapid and uniform heating of the precursors. The microwave-assisted process enhances reaction efficiency, promotes high-yield formation, and ensures the synthesis of nanostructured products with well-controlled morphology and high crystallinity [70]. Microwave-assisted methods have been widely used for the synthesis of g-$C_3N_4$-based materials, facilitating the rapid fabrication of composites and structurally modified systems with enhanced physicochemical and functional properties [71]. For instance, Xie et al. [72] fabricated oxygen-doped g-$C_3N_4$ with carbon vacancies (O-CNC) via a rapid microwave-assisted method (Figure 2a). Melamine–cyanuric acid (MCA) and oxalic acid were used as the precursors. Initially, 1 g of MCA was mixed with a specific amount of oxalic acid in an alumina crucible. The crucible was then placed in a larger crucible containing graphite powder, which served as a microwave absorber. The resulting O-CNC exhibited a mesoporous nanosheet structure with an approximate thickness of 20 nm. The specific surface area of the prepared sample was determined to be 59.75 $m^2\ g^{-1}$. Similarly, Yamini et al. [73] prepared a g-$C_3N_4$/$WO_3$ nanocomposite through the microwave-assisted approach. In this synthesis, melamine and tungsten chloride were used as precursors for g-$C_3N_4$ and $WO_3$, respectively. Glycerol acted as the reaction medium, while glucose functioned as a reducing agent. The as-synthesized nanocomposite demonstrated an average crystallite size of 10.864 nm and a specific surface area of 40.78 $m^2\ g^{-1}$. The optical bandgap, calculated from the Kubelka–Munk plot, was found to be 2.4 eV. FESEM analysis revealed that the as-prepared sample consisted of uniformly distributed cube-like structures dispersed over sheet-like morphologies. Furthermore, Hoang et al. [74] prepared a Pd-decorated g-$C_3N_4$ (Pd/g-$C_3N_4$) photocatalyst by a microwave-assisted wet-chemical reduction method. Palladium chloride was used as the precursor for Pd nanoparticles. The obtained Pd/g-$C_3N_4$ was composed of thin g-$C_3N_4$ nanosheets uniformly decorated with well-dispersed Pd nanoparticles, with an average particle size of approximately 5.7 nm. The composite exhibited a bandgap energy

of 2.72 eV and a BET surface area of 64 $m^2$ $g^{-1}$. Additionally, Zhang et al. [75] synthesized an Ag/ZnO/g-$C_3N_4$ ternary composite via a microwave-assisted approach. Ultrathin g-$C_3N_4$ nanosheets were first prepared via an ultrasonic exfoliation method, after which Ag nanoparticles and ZnO micro/nanorods were introduced to synthesize a ternary heterostructure. The resulting composite exhibited a narrowed bandgap of 2.92 eV, compared with pristine ZnO (3.24 eV) and g-$C_3N_4$ (3.08 eV), indicating improved light absorption and enhanced photocatalytic performance. Matias et al. [76] synthesized g-$C_3N_4$/$TiO_2$ via a microwave-assisted method (Figure 2b). XRD analysis confirmed the coexistence of anatase $TiO_2$ and g-$C_3N_4$ without impurity phases, while electron microscopy revealed ultrafine $TiO_2$ nanocrystals uniformly anchored on two-dimensional g-$C_3N_4$ nanosheets, forming a well-defined interfacial heterojunction.

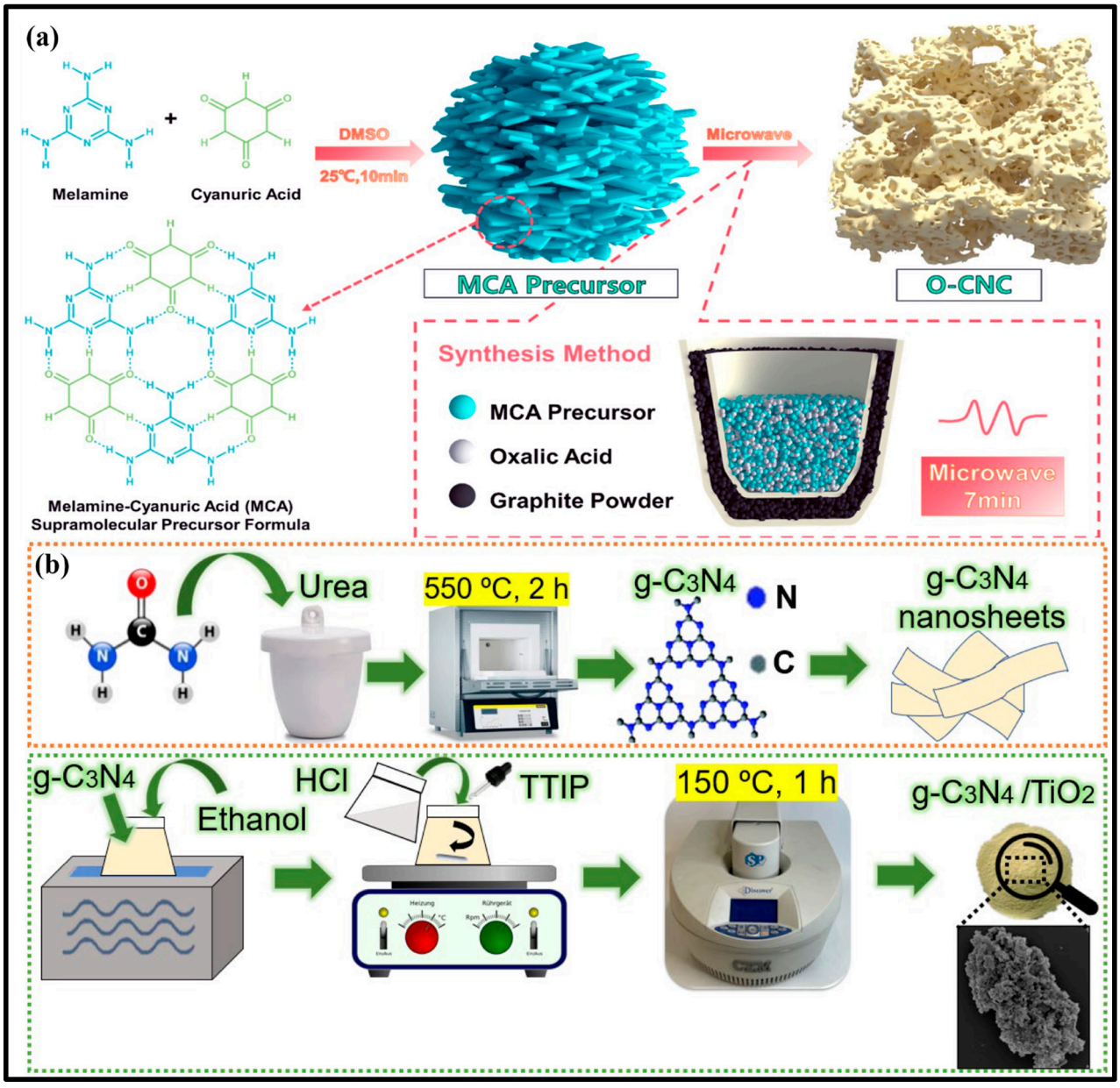



**Figure 2.** (**a**) Diagrammatic representation of the preparation method for oxygen-doped g-$C_3N_4$ with carbon vacancies (O-CNC). Reprinted with permission from [72]. Copyright 2021, American Chemical Society. (**b**) Microwave-assisted fabrication of g-$C_3N_4$/$TiO_2$ heterostructures. Figure reprinted from [76], which is open access and permits unrestricted use of the material under the terms of the creative commons CC-BY.

2.2.3. Calcination Method

Calcination is a thermally induced process in which materials are heated to elevated temperatures below their melting point to induce specific physical and chemical changes. This method is commonly used to remove adsorbed moisture, expel volatile components, and induce partial or complete oxidation of materials [77]. The calcination process is generally carried out under controlled atmospheric conditions to precisely regulate structural, morphological, and compositional changes [78]. Owing to its simplicity, cost-effectiveness, and scalability, calcination is extensively employed in the synthesis of nanomaterials and photocatalysts. For instance, Lan et al. [79] prepared mesoporous g-$C_3N_4$ via a calcination-assisted method utilizing ammonium sulfate and melamine as precursors (Figure 3a). Briefly, the precursors were dispersed in ethanol, followed by stirring, drying, and subsequent calcination at 550 °C for 3 h. After cooling and grinding, mesoporous g-$C_3N_4$ was obtained. The resulting mesoporous g-$C_3N_4$ exhibited a specific surface area of 32.65 $m^2$ $g^{-1}$, which is approximately 4.4-fold higher than that of bulk g-$C_3N_4$. The enhanced surface area indicates that calcination effectively modifies the porous structure of g-$C_3N_4$, thereby increasing the availability of active sites for photocatalytic reactions. Similarly, Cao et al. [80] used a facile calcination technique to synthesize $SnO_2$/g-$C_3N_4$ nanocomposites. The synthesized composite exhibited a higher surface area than pure $SnO_2$. Specifically, the composite with 7 wt% g-$C_3N_4$ achieved a BET surface area of 132.5 $m^2$ $g^{-1}$, providing more active sites for gas adsorption. These findings highlight the importance of optimizing the g-$C_3N_4$ content to achieve favorable structural properties and improved performance. Furthermore, Liu et al. [81] synthesized silver-modified graphitic carbon nitride (Ag/CN-x) via a simple calcination method using silver ammonia solution and dicyandiamide as starting materials (Figure 3b). A series of Ag/CN-x photocatalysts was prepared by varying the calcination time from 1 to 10 h to investigate its effect on photocatalytic activity. The Ag/CN-8 sample exhibited the highest methyl orange degradation efficiency (98.6%) under visible-light irradiation, indicating that an appropriate calcination time is essential for maximizing the photocatalytic performance of Ag/g-$C_3N_4$ composites. Wang et al. [82] fabricated a $TiO_2$@C/g-$C_3N_4$ Z-scheme heterojunction using a one-step calcination method. The as-synthesized material exhibited an accordion-like multilayer morphology with open interlayer spaces. XRD analysis confirmed the coexistence of anatase and rutile phases of $TiO_2$ along with g-$C_3N_4$, indicating the successful formation of the heterostructure. The composite also showed a narrowed bandgap of 2.69 eV, which improved charge separation and enhanced photocatalytic removal of nitric oxide (NO). Furthermore, Shin et al. [83] synthesized g-$C_3N_4$/$Co_3O_4$ composites via a one-pot calcination method. Melamine, urea, and cobalt chloride hexahydrate were used as precursors. The as-prepared g-$C_3N_4$/$Co_3O_4$ exhibited a BET surface area and pore diameter of 20.45 $m^2$ $g^{-1}$ and 44.73 nm, respectively. Moreover, the material possessed a hybrid porous sponge-like structure resulting from the hybridization of two-dimensional (2D) porous g-$C_3N_4$ and octahedral $Co_3O_4$ particles.

Overall, the reported studies indicate that calcination temperature is a key parameter influencing the physicochemical properties and photocatalytic performance of g-$C_3N_4$-based materials. In general, increasing the calcination temperature promotes the polycondensation of nitrogen-rich precursors, resulting in improved crystallinity and more efficient charge separation. Moderate calcination temperatures are associated with the development of a porous structure and a higher specific surface area, which provide more accessible active sites for PMS activation and pollutant adsorption. However, excessively high temperatures or prolonged calcination may lead to partial decomposition of the g-$C_3N_4$ framework, collapse of the porous structure, and particle sintering, thereby reducing the surface area and limiting photocatalytic performance. Therefore, careful optimization of the calcination temperature is essential to achieve an appropriate balance between

crystallinity, porosity, and charge-transfer properties, ultimately enhancing the overall photocatalytic degradation efficiency of g-$C_3N_4$-based materials.

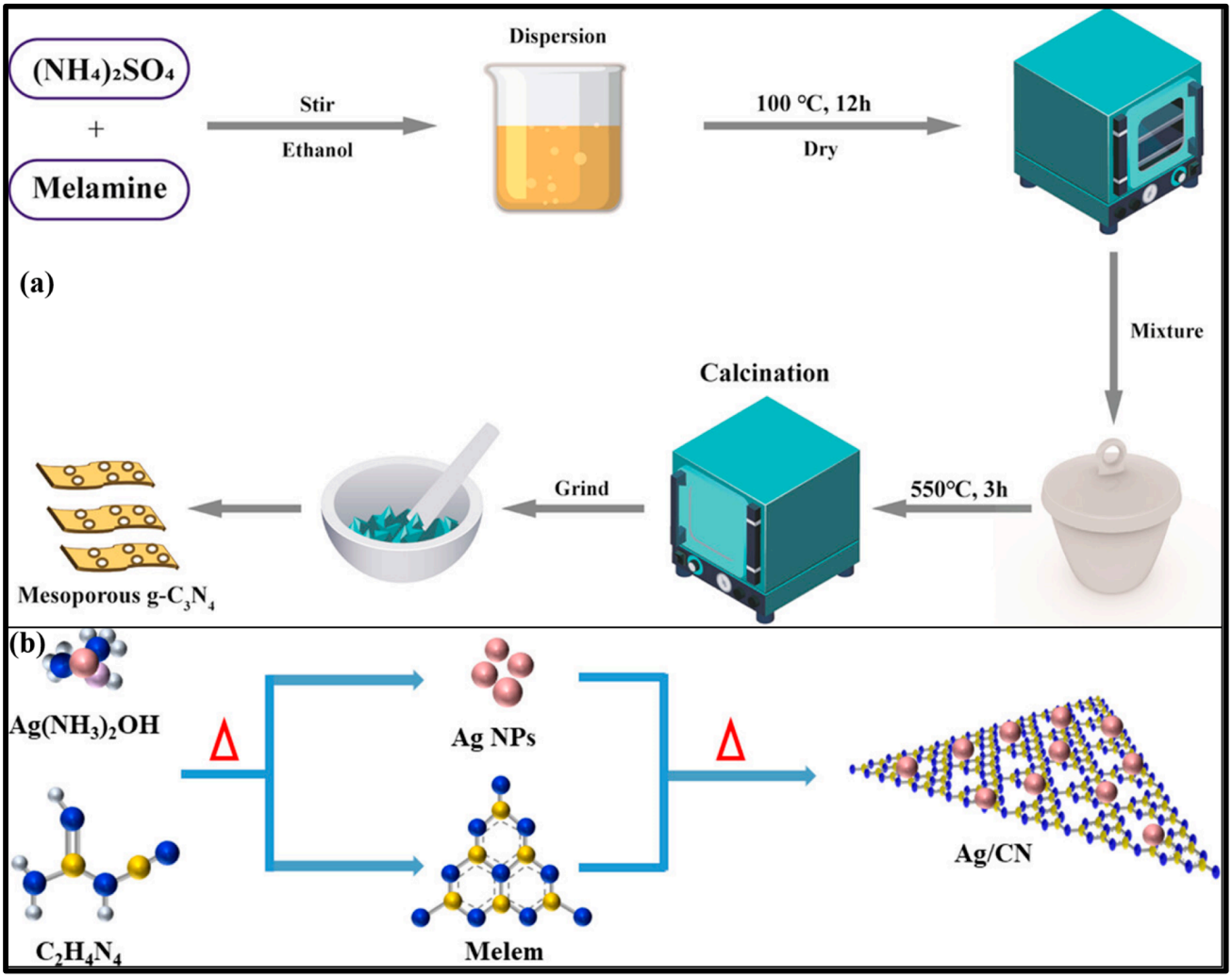



**Figure 3.** (**a**) Preparation pathway of mesoporous g-$C_3N_4$. Reprinted from [79] which is open access and permits unrestricted use of materials under the terms of the Creative Commons CC-BY. (**b**) Schematic representation of the preparation process of Ag/CN-x. Reprinted from [81] which is open access and permits unrestricted use of materials under the terms of the Creative Commons CC-BY.

#### 2.2.4. Sol–Gel Method

The sol–gel method is a simple, versatile, and cost-effective strategy commonly used for the preparation of nanomaterials. In this method, solutes are dispersed in a solvent to form a colloidal sol. As the reaction proceeds, the sol gradually transforms into a three-dimensional network, known as a gel. The resulting gel is then subjected to drying and thermal treatment to produce the final solid product [84,85]. The sol–gel method enables precise control over morphology, particle size, porosity, and composition, and also facilitates doping and structural modifications of materials. Owing to these advantages, it is widely used for the preparation of g-$C_3N_4$-based materials [86]. For instance, Panimalar et al. [87] synthesized $MnO_2$/g-$C_3N_4$ heterostructure via a sol–gel method followed by an annealing process. During synthesis, urea, potassium permanganate, and manganese (II) sulfate were used as precursors. Different amounts of g-$C_3N_4$ (25, 50, and 100 mg) were added to adjust the $MnO_2$/g-$C_3N_4$ ratio, and the obtained samples were labeled as MG1, MG2, and MG3, respectively. Among these, MG3 exhibited the highest photocatalytic activ-

ity. The MG3 composite consisted of spherical $MnO_2$ nanoparticles with diameters ranging from 25 to 40 nm, uniformly dispersed over g-$C_3N_4$ nanosheets, with a high surface area of 105.21 $m^2$ $g^{-1}$. These results demonstrate that the sol–gel method facilitates the formation of well-dispersed heterostructures with enhanced photocatalytic performance. Similarly, Kumar et al. [88] employed the sol–gel method to synthesize g-$C_3N_4$/$TiO_2$/$Fe_3O_4$@$SiO_2$ heterojunction. $Fe_3O_4$@$SiO_2$ were dispersed in 2-propanol under sonication, and the pH was adjusted to 8–9 using $NH_3$ solution. Subsequently, titanium (IV) butoxide (TBOT) and ultrathin g-$C_3N_4$ nanosheets were introduced, and the suspension was stirred at 80 °C for 16 h. The resulting product was washed and dried, and calcined at 400 to 600 °C to obtain the final composite. The crystallite sizes of the prepared catalyst were 3.2, 3.68, and 8.77 nm at calcination temperatures of 400, 500, and 600 °C, respectively. The synthesized nanocomposite was applied as photocatalyst for the degradation of ibuprofen. The highest ibuprofen degradation efficiency (98%) was achieved at 500 °C, indicating that appropriate calcination temperature enhances crystallinity, thereby significantly improving photocatalytic performance. Furthermore, Wu et al. [89] synthesized g-$C_3N_4$/$TiO_2$ S-scheme heterojunction via one-step sol–gel method using urea as a precursor. The as-synthesized nanocomposite consisted of uniformly dispersed nanoparticles with diameters ranging from 20 to 50 nm. In another study, a mesoporous $SnO_2$-$TiO_2$@g-$C_3N_4$ nanosorbent was fabricated using an ultrasound-assisted sol–gel method followed by calcination [90]. Initially, Sn-$TiO_2$ was synthesized from $SnCl_4 \cdot 5H_2O$ and Titanium (IV) isopropoxide, whereas g-$C_3N_4$ was obtained from urea. The as-synthesized nanosorbent exhibited a BET surface area, average pore size, and total pore volume of 180 $m^2$ $g^{-1}$, 2.73 nm, and 0.37 $cm^3$ $g^{-1}$, respectively. The high surface area of the nanosorbent enabled efficient Pb (II) removal from contaminated water, resulting in a remarkable adsorption capacity of 927.6 mg/g. Similarly, Glazar et al. [91] synthesized Ag/$TiO_2$/g-$C_3N_4$ nanocomposites via in-situ sol–gel deposition strategy (Figure 4a). In this approach, g-$C_3N_4$ was dispersed in isopropanol, titanium (IV) isopropoxide (TTIP) and $AgNO_3$ were used as $TiO_2$ and Ag precursors, respectively. Moreover, L-ascorbic acid was employed as reducing agent to promote the in-situ growth of Ag/$TiO_2$ on g-$C_3N_4$ surface. In another study, Zhang et al. [92] synthesized g-$C_3N_4$/$TiO_2$ heterostructures via a modified sol–gel method followed by calcination (Figure 4b). Initially, g-$C_3N_4$ nanosheets were prepared through the thermal polymerization of urea at 550 °C. Subsequently, amorphous $TiO_2$ was grown in situ on the g-$C_3N_4$ nanosheets using tetrabutyl titanate (TBT) as the titanium precursor in ethanol suspension. Finally, the composite was annealed at 460 °C to obtain the g-$C_3N_4$/$TiO_2$ heterostructure, which exhibited a specific surface area of 120.35 $m^2$/g.

#### 2.2.5. Green Synthesis

Green synthesis has recently emerged as an eco-friendly and sustainable strategy for the fabrication of nanomaterials. Owing to its environmentally friendly nature, this approach reduces dependence on toxic chemicals and supports the core principles of green chemistry, including waste minimization and the use of renewable resources. Various biological materials such as plant extracts, bacteria, fungi, and other microorganisms are used as natural reducing and stabilizing agents during synthesis. As a result, the process is eco-friendly, less expensive, and safer than conventional synthesis methods. Furthermore, green synthesis has also been applied to prepare of g-$C_3N_4$-based materials [93,94]. For instance, Ho et al. [94] synthesized g-$C_3N_4$/$CeO_2$ using the green synthesis approach, in which the leaf extract of *Cleistocalyx operculatus* (CE) acted as both a reducing and capping agent. The synthesized nanocomposite exhibited a nanoflake morphology, with a thickness of around 10 nm and a lateral size of more than 100 nm. The average crystallite size, surface area, and pore size of the synthesized nanocomposite were reported to be 7.5 nm,

130 $m^2$ $g^{-1}$, and 1.94 nm, respectively. Similarly, Khan et al. [95] synthesized a $TiO_2$/g-$C_3N_4$ nanocomposite using an extract of *Zingiber officinale*. Initially, green-modified g-$C_3N_4$ (GCN) was synthesized by adding 1 g of *Zingiber officinale* extract to 2 g of chemically prepared g-$C_3N_4$ in an ethanol–water mixture, followed by hydrothermal treatment at 150 °C for 4 h and subsequent calcination at 500 °C for 3 h. Meanwhile, $TiO_2$ nanoparticles were prepared via a hydrothermal approach using titanium butoxide [$Ti(OBu)_4$] and anhydrous ethanol. Finally, the nanocomposite was fabricated by mixing different mass percentages (1, 3, 5, and 7%) of $TiO_2$ nanoparticles with 1 g of the prepared GCN in the ethanol–water solvent system. The synthesized nanocomposite exhibited a nanosheet-like morphology and a significantly enhanced surface area, which improved its visible-light photocatalytic performance.

Furthermore, Sofia et al. [96] employed an eco-friendly green synthesis method to synthesize an rGO/$TiO_2$/g-$C_3N_4$ ternary nanocomposite. In this study, leaf extract of *Plectranthus amboinicus* (karpooravalli) was used as both a reducing and a stabilizing agent. The prepared nanocomposite consisted of spherical nanoparticles decorated with plate-like surfaces, which enhanced the catalytic surface area. The ternary nanocomposite exhibited an average crystallite size of 15.04 nm. Furthermore, the bandgap of rGO/$TiO_2$/g-$C_3N_4$ was found to be 2.5 eV compared with those of pure rGO (3.2 eV) and rGO/$TiO_2$ (2.7 eV). The reduced bandgap enabled 98.5% degradation of methylene blue under visible-light irradiation by enhancing visible-light absorption and facilitating charge transfer across the ternary heterojunction.

Despite its environmental advantages, green synthesis still faces several challenges that limit its wider application. Most reported studies have primarily focused on improving the photocatalytic performance of g-$C_3N_4$-based materials, whereas quantitative sustainability indicators, such as energy consumption, carbon footprint, and comprehensive life cycle assessments, are rarely evaluated. In addition, the use of biological precursors may introduce variations in the composition of the synthesized materials, thereby affecting reproducibility and making process standardization and large-scale production more challenging. Furthermore, many green synthesis protocols still involve energy-intensive steps, such as hydrothermal treatment and calcination, which partially offset their environmental benefits. Therefore, future research should place greater emphasis on systematically evaluating the sustainability, reproducibility, scalability, and overall environmental impact of green synthesis to facilitate its practical application [97].

#### 2.2.6. Other Methods

In addition to hydrothermal, sol–gel, and green synthesis approaches, several other techniques have been used for the preparation of g-$C_3N_4$ and its composite materials. For example, chemical vapor deposition (CVD) is an important method in which solid deposits are formed through chemical reactions between gaseous precursors and a substrate surface [98]. Using the CVD method, Lv et al. synthesized P-doped ultrathin g-$C_3N_4$ microspheres (P/UH-CNS) [99]. The synthesized material exhibited a significantly increased specific surface area of 207 $m^2$ $g^{-1}$ along with a reduced bandgap of 2.2 eV. The high surface area and narrowed bandgap contributed to enhanced visible-light photocatalytic activity, demonstrating the effectiveness of the CVD method in tailoring the structural and optical properties of g-$C_3N_4$-based materials. Similarly, Luo et al. [100] synthesized g-$C_3N_4$ nanosheets via a green ball-milling strategy (Figure 4c). In this approach, bulk g-$C_3N_4$, obtained by the thermal polymerization of melamine, was ball-milled with different solvents (isopropanol, ethanol, or deionized water) under optimized milling conditions to produce ultrathin g-$C_3N_4$ nanosheets with enhanced photocatalytic performance.Additionally, Ismael et al. [101] prepared Ni-doped g-$C_3N_4$ photocatalysts via a simple ultrasonic-assisted

approach. Using this method, nickel acetate was used as the nickel precursor, while melamine served as the source of g-$C_3N_4$. A series of Ni-doped samples with different nickel contents (1.5, 2.4, 4.7, 11, and 20 wt%) were prepared and labeled as 1.5 NiCN, 2.4 NiCN, 4.7 NiCN, 11 NiCN, and 20 NiCN, respectively. The corresponding bandgap energies were found to be 2.77, 2.79, 2.77, 2.60, 2.49, and 2.20 eV, respectively. These results demonstrate that increasing the nickel content effectively tailors the optical properties of g-$C_3N_4$, ultimately leading to enhanced photocatalytic performance.

In summary, hydrothermal methods are commonly used for the preparation of g-$C_3N_4$-based photocatalysts because they enhance interfacial contact between components and improve charge separation. The sol–gel method facilitates the formation of uniform and porous structures, whereas green synthesis provides an eco-friendly and cost-effective approach by utilizing natural extracts to prepare functional materials. Overall, the selection of synthesis method depends on the desired structure, physicochemical properties, and intended photocatalytic applications. The advantages and limitations of the commonly used synthesis methods are summarized in Table 1.

**Table 1.** Comparison of the advantages and limitations of various synthesis methods used for the preparation of g-$C_3N_4$-based photocatalysts.

| Synthesis Method | Advantages | Limitations | References |
| --- | --- | --- | --- |
| Hydrothermal | 1. Enables precise control over nanoparticle size and morphology.<br>2. Produces highly crystalline materials with improved structural properties.<br>3. Suitable for synthesizing a wide variety of nanomaterials, including metal oxides, hydroxides, and sulfides.<br>4. Produces nanomaterials with high surface areas and enhanced photocatalytic performance. | 1. Crystal growth cannot be directly monitored during the synthesis process.<br>2. Requires high-pressure autoclave equipment, increasing synthesis costs.<br>3. Careful optimization of reaction conditions is required to achieve the desired material properties.<br>4. Not suitable for materials that are unstable under high-temperature and high-pressure conditions. | [102,103] |
| Microwave-assisted method | 1. Provides rapid and uniform heating, significantly reducing synthesis time compared with conventional methods.<br>2. Enables rapid nucleation and controlled crystal growth through uniform volumetric heating.<br>3. Improves energy efficiency and enables the use of environmentally friendly solvents such as water or ethanol. | 1. Limited microwave absorption by some precursors and solvents may restrict its applicability to certain materials.<br>2. Requires specialized microwave reactors, which increase equipment costs.<br>3. Scale-up for large-scale production remains technically challenging. | [69,104] |
| Calcination | 1. Enables thermal polymerization and phase transformation to obtain the desired material composition.<br>2. Effectively removes residual organic species and volatile impurities, improving material purity.<br>3. Facilitates the incorporation of dopants and the formation of stable heterojunctions through thermal treatment.<br>4. Compatible with a wide range of precursor materials and suitable for large-scale production. | 1. High temperatures may cause particle agglomeration and loss of porosity.<br>2. Excessive calcination can decrease the specific surface area and reduce the number of active sites.<br>3. Precise control of calcination temperature and duration is essential to prevent structural degradation. | [105] |
| Sol–gel | 1. Enables the preparation of homogeneous nanomaterials with high purity.<br>2. Produces materials with high surface areas and tunable pore structures.<br>3. Facilitates the fabrication of complex nanostructures and multicomponent composites at relatively low processing temperatures. | 1. The synthesis process is relatively time-consuming due to hydrolysis, gelation, and drying steps.<br>2. Careful optimization of synthesis parameters is required to ensure reproducibility.<br>3. The method is not universally applicable, as some materials are difficult to synthesize using the sol–gel route. | [106,107] |

**Table 1.** *Cont.*

| Synthesis Method | Advantages | Limitations | References |
| --- | --- | --- | --- |
| Green synthesis | 1. Utilizes renewable biological resources, such as plant extracts or microorganisms, as reducing and stabilizing agents.<br>2. Eliminates or minimizes the use of hazardous chemicals, making the process environmentally friendly.<br>3. Offers a simple, cost-effective, and sustainable route for preparing functional nanomaterials. | 1. Limited control over nanoparticle size, morphology, and crystallinity compared with conventional synthesis methods.<br>2. Large-scale production remains challenging due to batch-to-batch variations and process standardization issues. | [97,108] |

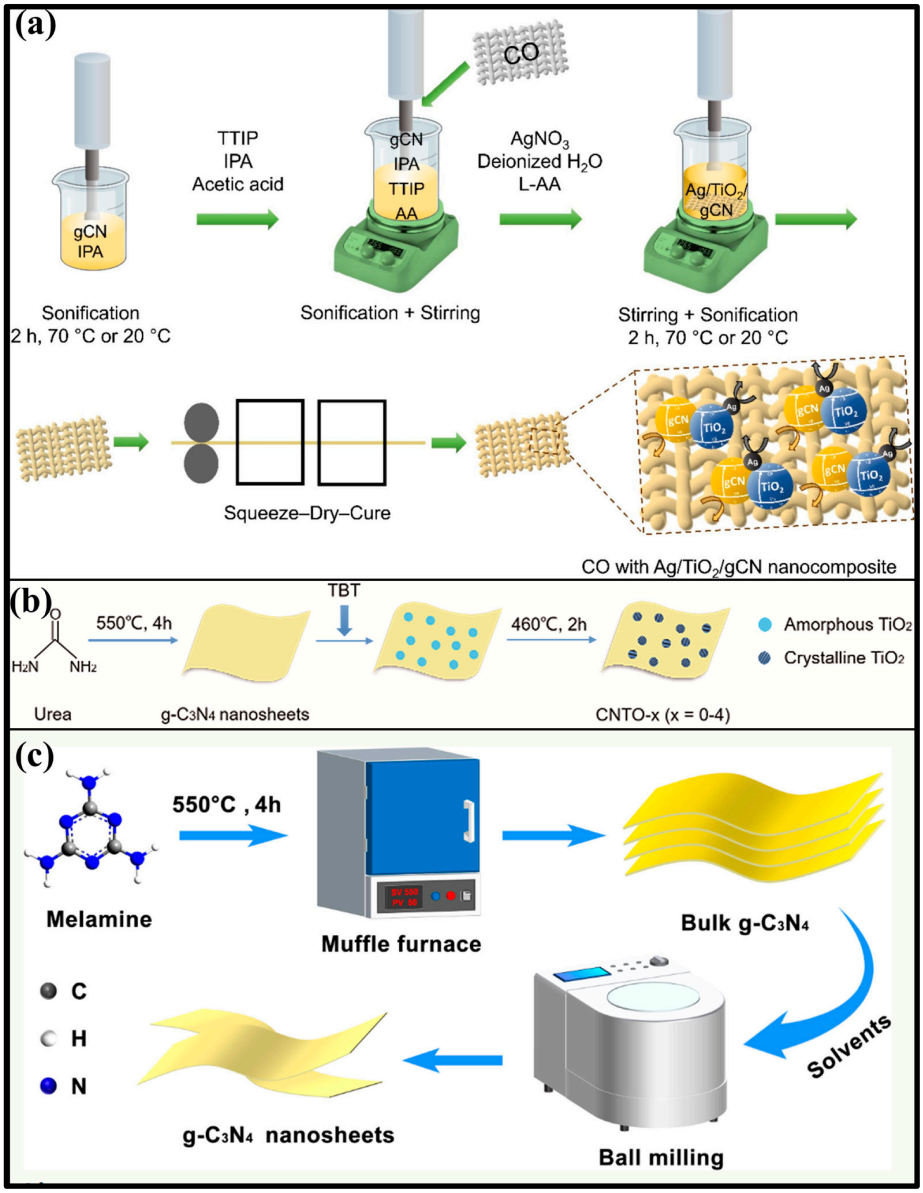



**Figure 4.** (**a**) The schematic illustration of the in-situ synthesis of $Ag/TiO_2/g\text{-}C_3N_4$ on the CO substrate at 70 or 20 °C. Adapted from [91], which is open access and permits unrestricted use of the materials under the terms of the Creative Commons CC-BY. (**b**) Schematic representation of the synthesis of CNTO-x. Adapted from [92], which is open access and permits unrestricted use of the materials under the terms of the Creative Commons CC-BY. (**c**) Schematic representation of the preparation of $g\text{-}C_3N_4$ nanosheets via a green ball-milling strategy. Adapted with permission from [100], which is open access and permits unrestricted use under the terms of the Creative Commons CC BY license.

## 3. Mechanism of Organic Pollutants Degradation Using g-$C_3N_4$ and g-$C_3N_4$-Based Materials

The high photocatalytic performance of g-$C_3N_4$ and its composites originates from their unique electronic and structural properties, which facilitate the generation and efficient separation of electron–hole ($e^-$–$h^+$) pairs under visible-light irradiation. The presence of oxidants, such as peroxymonosulfate (PMS), further promotes the generation of reactive radicals. These features make g-$C_3N_4$-based materials highly effective for the photocatalytic degradation of organic pollutants, particularly antibiotics. Based on previous studies and the experimental findings [3,59,109–115], a possible mechanism for the photocatalytic removal of organic pollutants using g-$C_3N_4$ and its composites in the presence of PMS is proposed below.

When semiconductors (SCs) absorb incident light, the electrons ($e^-$) are excited from the valence band (VB) to the conduction band (CB), resulting in the generation of $e^-$–$h^+$ pairs. The electronic transition from VB to CB occurs when the energy of the incident photon is equal to or greater than the bandgap energy of the material, which is typically in the range of 2.7–2.8 eV (reaction (1)) [59]. The photogenerated electrons reduce PMS, producing highly reactive sulfate radicals ($SO_4^{\bullet-}$) and hydroxyl radicals ($^\bullet$OH) (reactions (2) and (3)). Meanwhile, the photogenerated holes ($h^+$) oxidize PMS to generate peroxymonosulfate radicals ($SO_5^{\bullet-}$) (reaction (4)). Moreover, electrons migrate to the surface of the photocatalyst and reduce oxygen molecules ($O_2$) to superoxide radical anions ($O_2^{\bullet-}$), which subsequently react with electrons to produce hydrogen peroxide ($H_2O_2$) (reactions (5) and (6)). Thereafter, $H_2O_2$ is reduced by electrons to generate $^\bullet$OH and hydroxide ions ($OH^-$) (reaction (7)) [115]. In addition, photogenerated $h^+$ react with water and $OH^-$ to generate $^\bullet$OH (reactions (8) and (9)). Moreover, additional $^\bullet$OH are produced through the reaction of $SO_4^{\bullet-}$ with water and $OH^-$ (reactions (10) and (11)). $HSO_5^-$ reacts with $SO_4^{\bullet-}$ and $^\bullet$OH, producing $SO_5^{\bullet-}$ along with $HSO_4^-$ and $H_2O$ (reactions (12) and (13)). These radicals (i.e., $SO_5^{\bullet-}$) decompose to regenerate two $SO_4^{\bullet-}$ radicles and produce oxygen molecules (reaction (14)). $O_2^{\bullet-}$ reacts with $^\bullet$OH and protons ($H^+$) to form singlet oxygen ($^1O_2$) and $H_2O_2$ (reactions (15) and (16)). Finally, reactive species, including $O_2^{\bullet-}$/$^\bullet$OH/$h^+$/$SO_4^{\bullet-}$, attack organic pollutants, specifically antibiotics, to convert them into final products such as $CO_2$, $H_2O$, and inorganic ions (reaction (17)). The schematic representations of photocatalytic removal of antibiotics through g-$C_3N_4$ and g-$C_3N_4$-based materials are illustrated in Figure 5a–e [109–113].

$$SC + hv \rightarrow h^+ + e^- \quad (1)$$

$$HSO_5^- + e^- \rightarrow SO_4^{\bullet-} + OH^- \quad (2)$$

$$HSO_5^- + e^- \rightarrow SO_4^{2-} + {}^\bullet OH \quad (3)$$

$$HSO_5^- + h^+ \rightarrow SO_5^{\bullet-} + H^+ \quad (4)$$

$$O_2 + e^- \rightarrow O_2^{\bullet-} \quad (5)$$

$$O_2^{\bullet-} + e^- + 2H^+ \rightarrow H_2O_2 \quad (6)$$

$$H_2O_2 + e^- \rightarrow OH^- + {}^\bullet OH \quad (7)$$

$$H_2O + h^+ \rightarrow {}^\bullet OH + H^+ \quad (8)$$

$$h^+ + OH^- \rightarrow {}^\bullet OH \quad (9)$$

$$SO_4^{\bullet-} + H_2O \rightarrow {}^\bullet OH + SO_4^{2-} + H^+ \quad (10)$$

$$SO_4^{\bullet-} + OH^- \rightarrow SO_4^{2-} + {}^\bullet OH \quad (11)$$

$$HSO_5^- + SO_4^{\bullet-} \rightarrow SO_5^{\bullet-} + HSO_4^- \quad (12)$$

$$HSO_5^- + {}^{\bullet}OH \rightarrow SO_5^{\bullet-} + H_2O \quad (13)$$

$$2SO_5^{\bullet-} \rightarrow 2SO_4^{\bullet-} + O_2 \quad (14)$$

$$O_2^{\bullet-} + {}^{\bullet}OH \rightarrow {}^1O_2 + OH^- \quad (15)$$

$$2O_2^{\bullet-} + 2H^+ \rightarrow H_2O_2 + {}^1O_2 \quad (16)$$

$$O_2^{\bullet-}/{}^{\bullet}OH/h^+/SO_4^{\bullet-} + \text{antibiotics} \rightarrow \text{degradation products} \rightarrow H_2O + CO_2 + \text{inorganic ions} \quad (17)$$

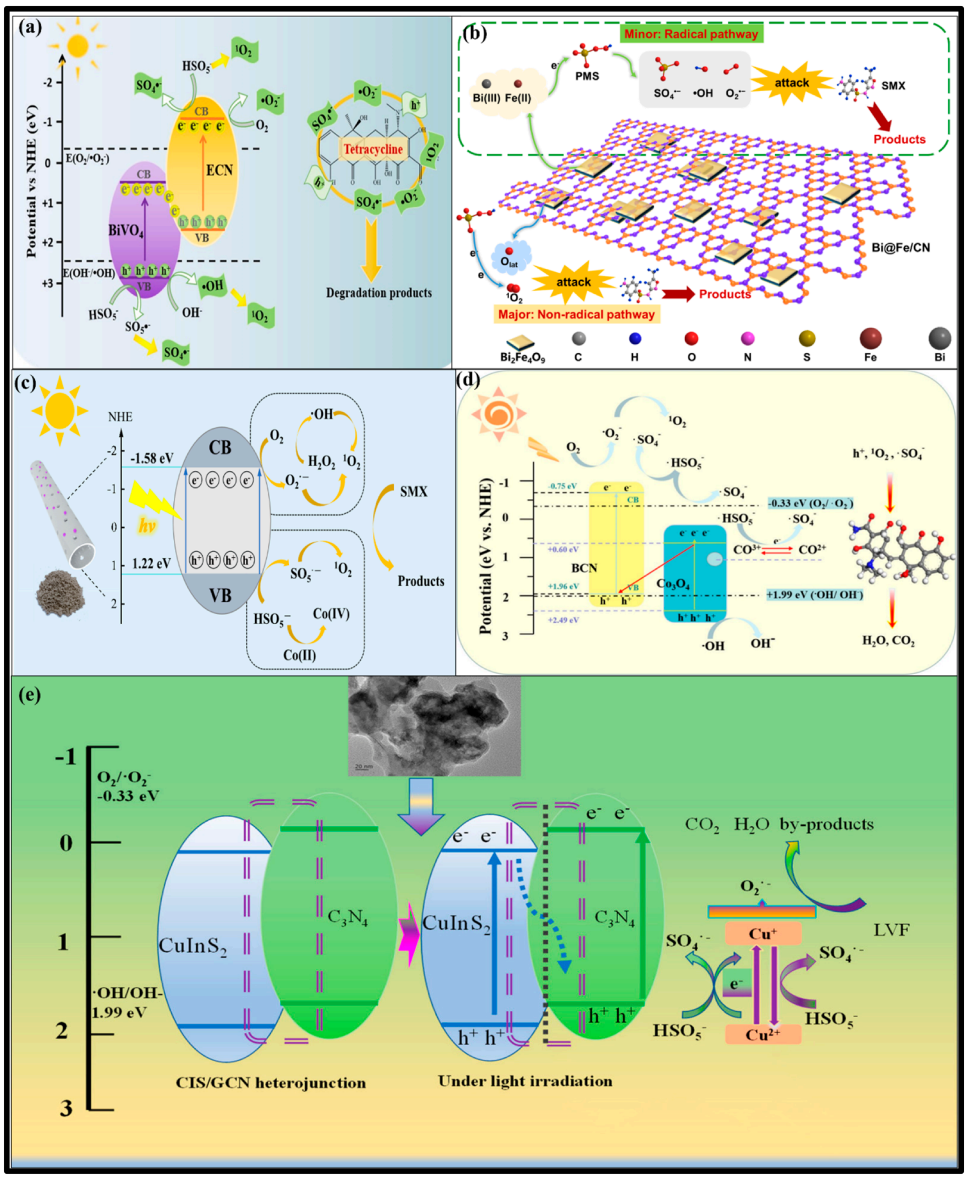



**Figure 5.** Proposed mechanisms for the visible-light-driven photocatalytic degradation of antibiotics via PMS activation over g-$C_3N_4$-based photocatalysts: (**a**) tetracycline (TC) via the $BiVO_4$/exfoliated g-$C_3N_4$ heterojunction. Reprinted with permission from [109]. Copyright 2022 American Chemical Society. (**b**) Sulfamethoxazole (SMX) over Bi@Fe/CN. Reprinted from [110], which is open access and permits unrestricted use of materials under the terms of the Creative Commons CC-BY. (**c**) SMX using Co-CN. Reprinted with permission from [111]. Copyright 2024 American Chemical Society. (**d**) Tetracycline (TC) via $Co_3O_4$/g-$C_3N_4$ heterojunction. Reprinted with permission from [112]. Copyright 2025 American Chemical Society. (**e**) Levofloxacin (LVF) over the $CuInS_2$/g-$C_3N_4$. Reprinted from [113], which is open access and permits unrestricted use of materials under the terms of the Creative Commons CC-BY.

*Mechanistic Verification, Degradation Intermediates and Mineralization*

In PMS-assisted photocatalytic degradation, the complete detoxification of the parent antibiotic cannot be guaranteed solely by its disappearance, as several intermediate products may be formed before complete mineralization. The intermediates are typically generated through hydroxylation, demethylation, deamination, defluorination, decarboxylation, ring opening, and C–N or C–C bond cleavage. Hence, identifying degradation intermediates is important for understanding the degradation pathways and assessing the environmental safety of treated water. Transformation products are usually identified using analytical techniques such as LC-MS, HPLC-MS, GC-MS, and UPLC-QTOF-MS based on their mass-to-charge (m/z) ratios. For instance, Zhang et al. [116] proposed the intermediates and degradation pathways of tetracycline in the CdS/g-$C_3N_4$/PMS/visible-light system, as illustrated in Figure 6. Similarly, Wang et al. [114] identified the degradation intermediates of ciprofloxacin in the Co/g-$C_3N_4$/PMS system and further evaluated the toxicity of the resulting products. Similarly, Lu et al. proposed the tetracycline degradation pathways and assessed the toxicity evolution of intermediates in an $MnO_2$@g-$C_3N_4$/PMS photocatalytic system [117].

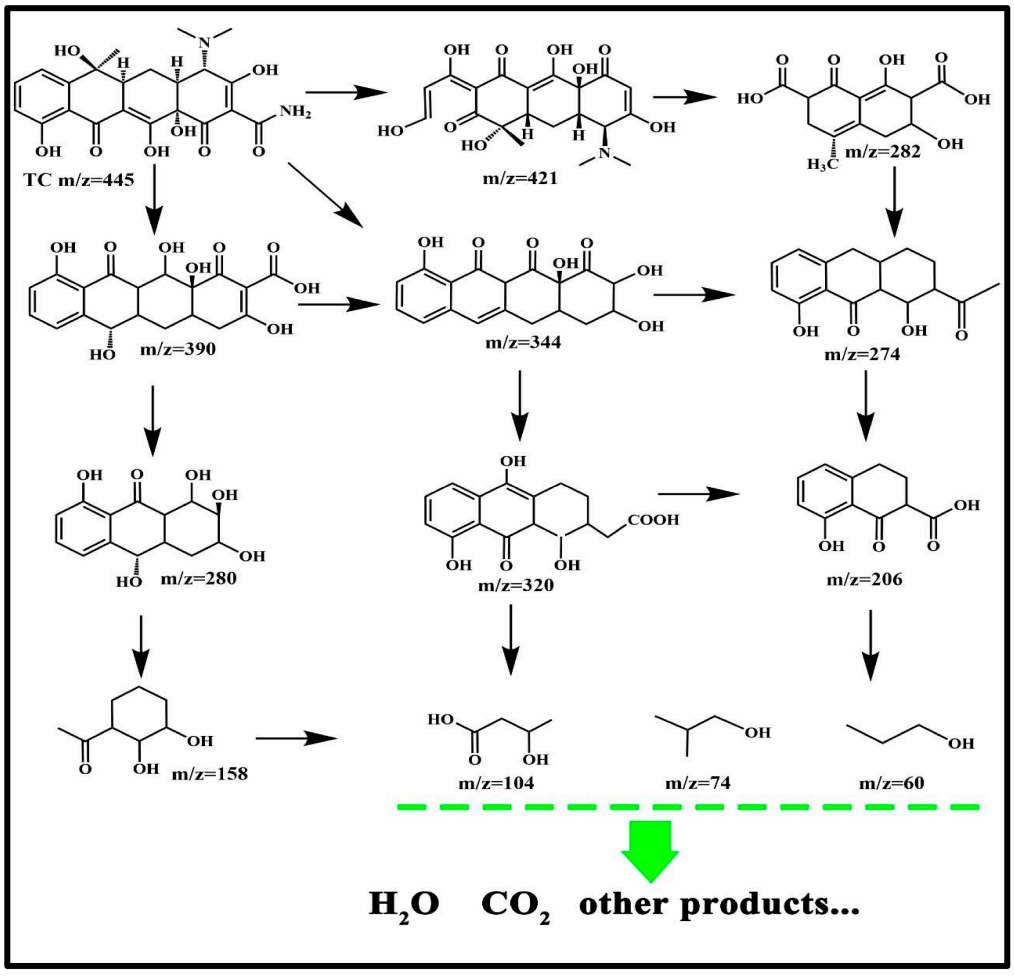



**Figure 6.** Possible degradation pathway of tetracycline (TC) in the CdS/g-$C_3N_4$/visible-light photocatalytic system. Reprinted with permission from [116]. Copyright 2024, American Chemical Society.

Complete mineralization is one of the primary goals in the degradation of antibiotics, as it indicates the conversion of organic pollutants and their intermediates into $CO_2$, $H_2O$, and inorganic ions. However, high a removal efficiency of the parent antibiotic does not necessarily indicate complete mineralization. In many photocatalytic PMS systems, the parent

antibiotic is rapidly degraded during the initial stage of the reaction, whereas the removal of total organic carbon (TOC) is slower, since the aromatic rings, heterocyclic structures and short-chain organic acids require further oxidation. Hence, TOC reduction, chemical oxygen demand (COD) removal, and inorganic ion release should be evaluated and discussed alongside degradation efficiency and kinetic parameters, where available. For instance, Lu et al. [117] found that the $MnO_2$@g-$C_3N_4$/PMS system achieved remarkable tetracycline degradation and 81.3% TOC removal after 180 min, suggesting that PMS-assisted g-$C_3N_4$-based photocatalysis can facilitate not only antibiotic transformation but also partial-to-substantial mineralization.

Experimental evidence, such as ESR/EPR analysis and radical scavenging tests, should be used to confirm the role of ROS in g-$C_3N_4$-based PMS-assisted photocatalytic systems. ESR/EPR spectroscopy with spin-trapping agents provides direct evidence of short-lived reactive species, whereas scavenger experiments are used to identify the major species involved in antibiotic degradation. The most widely used scavengers are methanol for both $^{\bullet}OH$ and $SO_4^{\bullet-}$, tert-butanol for $^{\bullet}OH$, p-benzoquinone for $O_2^{\bullet-}$, EDTA or triethanolamine for photogenerated holes, and sodium azide or furfuryl alcohol for $^1O_2$. For instance, Shi et al. demonstrated that $O_2^{\bullet-}$, $h^+$, $^1O_2$, $^{\bullet}OH$, and $SO_4^{\bullet-}$ were involved in the degradation of tetracycline in a Co-$C_3N_4$/PMS/visible-light system by radical trapping and ESR analysis [115]. In addition, Wang et al. demonstrated that $h^+$ and $O_2^{\bullet-}$ were the primary active species in ciprofloxacin degradation by Co/g-$C_3N_4$/PMS. Lu et al. found that $^{\bullet}OH$ and $SO_4^{\bullet-}$ were the major active species in tetracycline degradation by $MnO_2$@g-$C_3N_4$/PMS [114,117]. Hence, ESR and scavenger experiments should be considered essential for confirming ROS pathways in PMS-assisted g-$C_3N_4$ photocatalysis.

## 4. Application of g-$C_3N_4$-Based Materials for the Photocatalytic Degradation of Different Antibiotics

The uncontrolled release of antibiotic contaminants into aquatic environments has become a major global concern because of its harmful environmental impacts and contribution to antibiotic resistance [118]. Therefore, efficient and sustainable water purification technologies are urgently required for the removal of antibiotics from water. Among the various advanced water purification technologies, photocatalysis using g-$C_3N_4$-based materials has gained significant attention due to the superior chemical stability, suitable band structure, and environmentally benign nature [44,119]. Table 2 summarizes the photocatalytic degradation of antibiotics using g-$C_3N_4$-based photocatalysts, highlighting their role in peroxymonosulfate (PMS) activation, operating conditions, and corresponding degradation efficiencies.

Many researchers have investigated the application of g-$C_3N_4$-based materials for photocatalytic degradation of various antibiotics under different experimental conditions. For example, Guo et al. [120] fabricated Co/Fe-co-doped g-$C_3N_4$ (Co/Fe-CN) via thermal polymerization, producing an irregular flake-like morphology with a BET surface area of 55.76 $m^2\ g^{-1}$ and a bandgap of 2.84 eV. The Co/Fe-CN composite efficiently activated PMS under visible-light irradiation, achieving 92.1% levofloxacin (LVFX) degradation within 50 min under the optimum reaction conditions of 0.4 g/L catalyst, 1.0 mM PMS, pH 6.8, and an initial LVFX concentration of 20 mg/L. The degradation followed pseudo-first-order kinetics with an observed rate constant ($k_{obs}$) of 0.638 $min^{-1}$. Furthermore, the effect of catalyst dosage on the photocatalytic removal of LVFX was evaluated. As the catalyst dosage increased from 0.2 to 0.8 g/L, the degradation efficiency improved from 86.14 to 94.2%, while the corresponding rate constants were found to be approximately 1.5 times (for 0.8 g/L) higher than that at 0.2 g/L. Similarly, increasing the PMS concentration from 0.5 to 2.0 mM enhanced LVFX degradation due to increased $SO_4^{\bullet-}$ generation. However, only a

slight improvement was observed beyond 1.0 mM PMS, with degradation efficiencies of 92.1%, 94.6%, and 95.3% at 1.0, 1.5, and 2.0 mM, respectively, owing to the scavenging of reactive radicals by excess PMS. These results indicate that optimizing both the catalyst dosage and PMS concentration is essential for achieving efficient LVFX degradation, as excessive amounts provide only limited improvement in photocatalytic performance.

In another study, Bai et al. [121] synthesized a g-$C_3N_4$/FeCu-LDH nanocomposite via thermal polycondensation followed by wet-chemical method. The as-prepared material was used as a photocatalyst for the removal of tetracycline (TC). The incorporation of FeCu-LDH nanosheets into g-$C_3N_4$ increased the BET surface area from 71.97 to 82.89 $m^2$ $g^{-1}$, providing more active sites for PMS activation. Consequently, the g-$C_3N_4$/FeCu-LDH/PMS system achieved 99% TC degradation within 30 min under the optimum reaction conditions of 20 ppm TC, 100 mg $L^{-1}$ catalyst, 0.5 mM PMS, and pH 5.0. The photocatalyst also maintained high degradation efficiencies (94–99%) over a broad pH range (2–10), owing to effective surface charge modulation and the pH-dependent ionization of TC, whereas a slight decline under strongly alkaline conditions was attributed to TC hydrolysis. These results indicate that the FeCu-LDH/g-$C_3N_4$ heterojunction enhances PMS activation by providing more active sites while maintaining excellent photocatalytic performance over a wide pH range. Similarly, Huang et al. [109] synthesized a $BiVO_4$/exfoliated g-$C_3N_4$ (ECN) Z-scheme heterojunction photocatalyst for visible-light-driven PMS activation and efficient tetracycline (TC) degradation. Under optimized experimental conditions ([catalyst dosage] = 1.0 g/L, $[TC]_0$ = 20 mg/L, pH = 6, and temperature = 298 K), the $BiVO_4$/ECN photocatalyst achieved 83.0% TC degradation within 30 min. The photocatalyst exhibited an apparent rate constant of 0.1278 $min^{-1}$, demonstrating significantly enhanced photocatalytic activity compared with pristine ECN and bulk g-$C_3N_4$ (Figure 7a,b). The enhanced performance was achieved at an optimum PMS concentration of 0.3 mM, whereas a further increase in PMS concentration did not improve degradation efficiency because excess PMS consumed reactive radicals and reduced the activation efficiency (Figure 7c). Furthermore, the $BiVO_4$/ECN heterojunction exhibited robust photocatalytic activity over a broad pH range (3–11), with slightly superior degradation performance under acidic conditions (Figure 7d).

In another study, Lu et al. [122] fabricated a Z-type $Co_9S_8$/g-$C_3N_4$ heterojunction photocatalyst using a hydrothermal approach. The as-prepared composite was employed for sulphamerazine (SMR) degradation through PMS activation. Under optimized experimental conditions, [SMR] = 20 mg $L^{-1}$, [photocatalyst] = 0.4 g $L^{-1}$, [PMS] = 0.8 mM, pH = 7, and reaction time of 40 min, the composite achieved a high SMR degradation efficiency of 93%, whereas only 86% degradation was observed in the absence of PMS. These results clearly demonstrate that coupling of photocatalysis with PMS activation significantly enhances pollutant degradation efficiency. Furthermore, a series of $Co_9S_8$/CN-X composites with different $Co_9S_8$ loadings (5, 10, 15, 20, and 40 wt.%) were synthesized to evaluate the effect of material composition on photocatalytic performance. The optimum $Co_9S_8$ loading of 15 wt.% provided sufficient heterojunction interfaces to facilitate efficient charge separation and PMS activation. However, further increasing the $Co_9S_8$ content to 20 and 40 wt.% may lead to nanoparticle aggregation, blockage of active sites, and the formation of charge recombination centers, thereby hindered charge transfer and reduced the overall photocatalytic performance. The $Co_9S_8$/CN-15/PMS system demonstrated the highest observed rate constant ($k_{obs}$ = 0.065 $min^{-1}$), exceeding those of g-$C_3N_4$/PMS and $Co_9S_8$/PMS by 11.8 and 8.4 times, respectively.

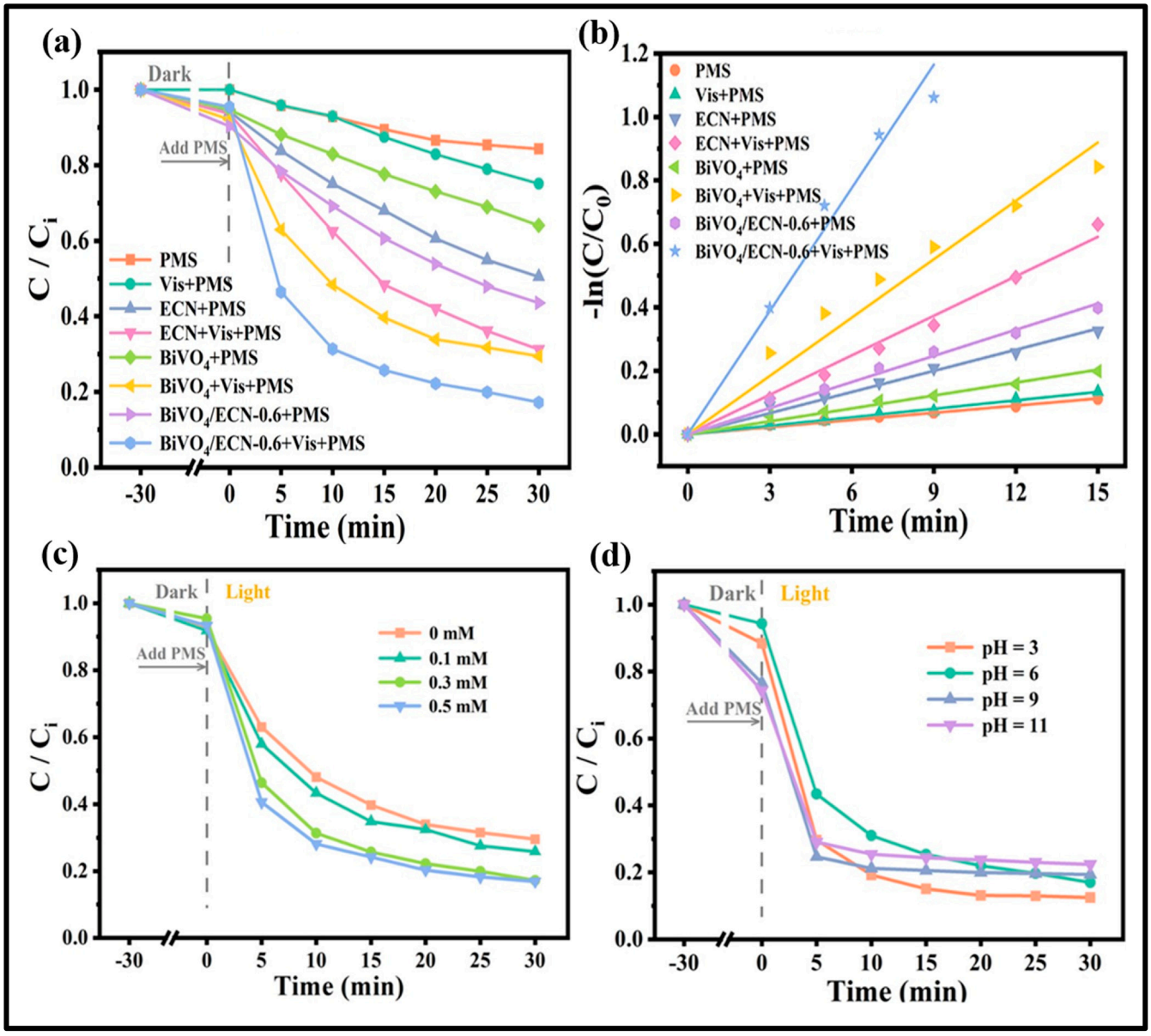



**Figure 7.** (**a**) Photocatalytic degradation of tetracycline (TC) under visible-light irradiation using different systems in the presence of PMS, (**b**) corresponding pseudo-first-order kinetic curves, (**c**) effect of PMS concentration on TC degradation, (**d**) effect of pH on TC degradation. Figure reprinted with permission from [109]. Copyright 2022 American Chemical Society.

Shi et al. [115] synthesized a carbonyl-modified g-$C_3N_4$ (CO-$C_3N_4$) photocatalyst via calcination method. The modified material (CO-$C_3N_4$) exhibited a higher specific surface area (47.97 $m^2$ $g^{-1}$) than pure g-$C_3N_4$ (27.93 $m^2$ $g^{-1}$), indicating enhanced surface properties. The as-prepared CO-$C_3N_4$ photocatalyst was employed for PMS activation to degrade tetracycline hydrochloride (TCH). Under the experimental conditions of [photocatalyst] = 0.2 g $L^{-1}$, $[TCH]_0$ = 10 mg $L^{-1}$, [PMS] = 200 mg $L^{-1}$, TCH removal efficiency of 97.77% was achieved within 60 min. The effects of different operational parameters were systematically investigated. Increasing the initial TCH concentration from 10 to 40 mg $L^{-1}$ resulted in a decline in removal efficiency from 97.77 to 79.77%, which was attributed to the limited availability of reactive radicals at fixed catalyst and PMS dosages. In contrast, increasing the catalyst dosage from 0.1 to 0.2 g $L^{-1}$ enhanced removal efficiency by providing more active sites for PMS activation. Furthermore, the influence of different water matrices, including reclaimed water, lake water, tap water, and deionized water,

was evaluated. The corresponding degradation efficiencies were 80.84, 84.24, 90.69, and 98.60%, respectively.

In addition, Tang et al. [123] synthesized Enteromorpha-derived biochar-modified g-$C_3N_4$ (BC/CN) via a two-step pyrolysis method by varying the biochar content. Among the as-prepared composites, BC/CN-15 exhibited the highest photocatalytic activity. Under the experimental conditions of, $[TC]_0$ = 10 mg $L^{-1}$, $[BC/CN\text{-}15]_0$ = 0.2 g $L^{-1}$, $[PMS]_0$ = 0.2 g $L^{-1}$, pH = 5.45, temperature = 293 K, approximately 90% tetracycline degradation was achieved within 60 min using visible-light irradiation, with a $k_{obs}$ value of 0.0355 $min^{-1}$. The BC/CN/PMS/Vis system also degraded oxytetracycline, chlortetracycline, ciprofloxacin, levofloxacin, and pefloxacin with degradation efficiencies of 85, 76, 59, 52, and 66%, respectively, corresponding to $k_{obs}$ values of 0.0313, 0.0114, 0.0144, 0.0225, and 0.0166 $min^{-1}$. These findings demonstrate that biochar modification effectively enhances PMS activation and broadens the applicability of g-$C_3N_4$-based photocatalysts for antibiotic degradation.

Nguyen et al. [124] synthesized boron and manganese-co-doped g-$C_3N_4$ (CNBMn) via a hydrothermal-assisted polymerization approach. The synthesis process involved $MnCl_2$, cyanuric acid, boric acid, and melamine as precursor materials (Figure 8a). By varying the $MnCl_2$ content (0.25, 0.5, and 0.75 mmol), three samples were prepared and labeled as CNBMn1, CNBMn2, and CNBMn3, respectively. Among these labeled samples, CNBMn2 showed superior properties, including a narrow bandgap of 2.50 eV and a BET surface area of 47 $m^2$ $g^{-1}$ (Figure 8b,c). This optimized sample was further applied for PMS activation during TC degradation, achieving 99% removal of TC under reaction conditions of 0.75 g $L^{-1}$ catalyst, 10 mg $L^{-1}$ TC, 1.5 mM PMS, and 40 min reaction time. Similarly, Xiao et al. [125] synthesized a Cu/Co/O-co-doped g-$C_3N_4$ photocatalyst via a simple one-step pyrolysis method. The as-synthesized photocatalyst was employed to activate PMS for the degradation of sulfamethoxazole (SMX) in aqueous solution. As shown in Figure 8d, the Cu/Co/O-g-$C_3N_4$/PMS system achieved 90% SMX degradation within 10 min, significantly outperforming pristine g-$C_3N_4$/PMS (14%) and O-doped g-$C_3N_4$/PMS (22%). The apparent rate constant was 0.631 $min^{-1}$ (Figure 8e). The enhanced catalytic performance was attributed to the synergistic effects of Cu–Co bimetallic doping and oxygen incorporation, which increased the density of active sites, facilitated charge transfer, and suppressed metal leaching.

Furthermore, using a thermal polymerization strategy, Wang et al. [114] synthesized a Co/g-$C_3N_4$ nanocomposite. The surface area and bandgap of the as-prepared material were 14.9461 $m^2$/g and 2.60 eV, respectively. The as-synthesized Co/g-$C_3N_4$ nanocomposite was used as a photocatalyst for PMS activation to degrade ciprofloxacin (CIP). The degradation efficiency of 88.87% was achieved using experimental conditions of [photocatalyst]= 100 mg/L, [CIP] = 10 mg/L, [PMS] = 0.6 mM, pH = 7.0, reaction time = 150 min and light source of 350 W xenon lamp. This study further demonstrated that the pH of reaction solution significantly affected PMS activation and CIP degradation efficiency. The maximum efficiency was achieved at a neutral pH (pH = 7). Under acidic conditions, the generated $SO_4^{\bullet-}$ readily reacted with excess $H^+$ to form $HSO_4^{\bullet-}$, thereby decreasing the concentration of reactive sulfate radicals available for ciprofloxacin degradation. In contrast, under alkaline conditions, $SO_4^{\bullet-}$ reacts with $OH^-$ to produce $^{\bullet}OH$, which possesses a lower oxidation potential than $SO_4^{\bullet-}$. Consequently, the reduced availability of $SO_4^{\bullet-}$ under acidic and alkaline conditions decreases the overall photocatalytic degradation efficiency of ciprofloxacin.

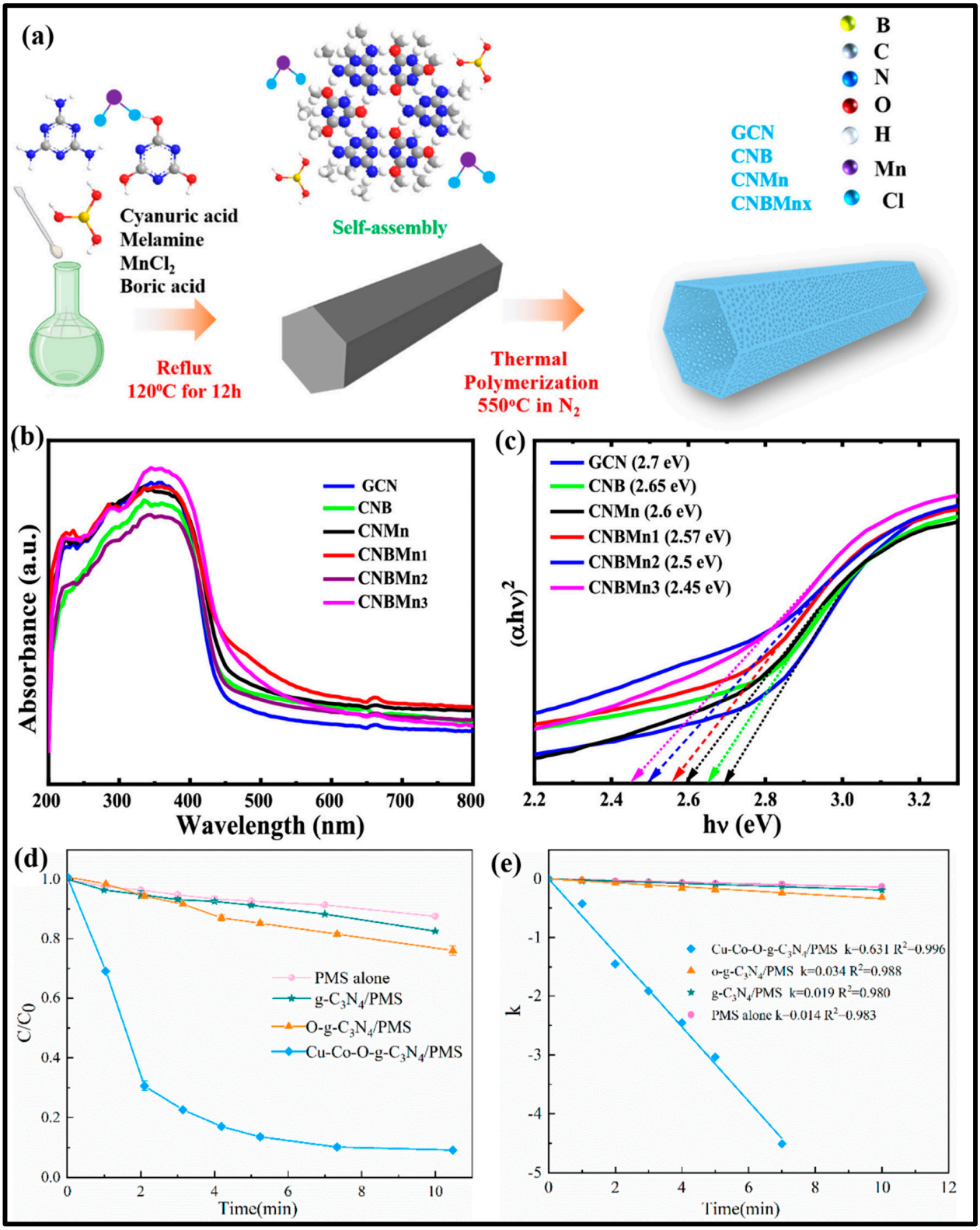



**Figure 8.** (**a**) Graphical representation of the synthesis procedure of CNBMn, (**b**) UV–visible diffuse reflectance spectra and (**c**) calculated bandgap energy of GCN, CNB, CNMn, and CNBMnx. Figure (**a**–**c**) reprinted from [124], which is open access and permits unrestricted use of materials under the terms of the creative commons CC-BY. (**d**) Effect of different systems on SMX degradation and (**e**) corresponding apparent reaction-rate constants (*k*) under different catalytic systems. Experimental conditions: catalyst dosage = 0.2 g $L^{-1}$, SMX concentration = 10 mg $L^{-1}$, PMS concentration = 0.8 mM, and temperature = 25 °C. Figure (**d**,**e**) reprinted from [125], which is open access and permits unrestricted use of materials under the terms of the creative commons CC-BY.

Hong et al. [126] fabricated S-scheme FeOOH/HCN via an in-situ precipitation method. The as-prepared nanocomposite was used as a photocatalyst for activation of PMS under visible-light irradiation for degradation of various antibiotics. The FeOOH/HCN/PMS/visible-light system achieved removal efficiencies of 82.2, 67.4, 88.9, and 86.4% for doxycycline hydrochloride, ciprofloxacin, tetracycline, and oxytetracycline, respectively. Additionally, Zhong et al. [113] developed a $CuInS_2$/g-$C_3N_4$ heterojunction for visible-light-assisted PMS activation towards levofloxacin (LVF) degradation. As shown in Figure 9a, PMS alone, catalyst adsorption, and visible-light photocatalysis showed limited contribution to LVF removal, while the combined visible-light/PMS/catalyst system achieved much faster degradation. The 3CIS/GCN/PMS system removed 98.9% of LVF within 60 min, demonstrating a strong synergistic effect between photocatalysis and PMS activation. This improved activity was mainly related to enhanced charge separation in the heterojunction, which promoted PMS activation and the generation of reactive oxygen species for antibiotic degradation.

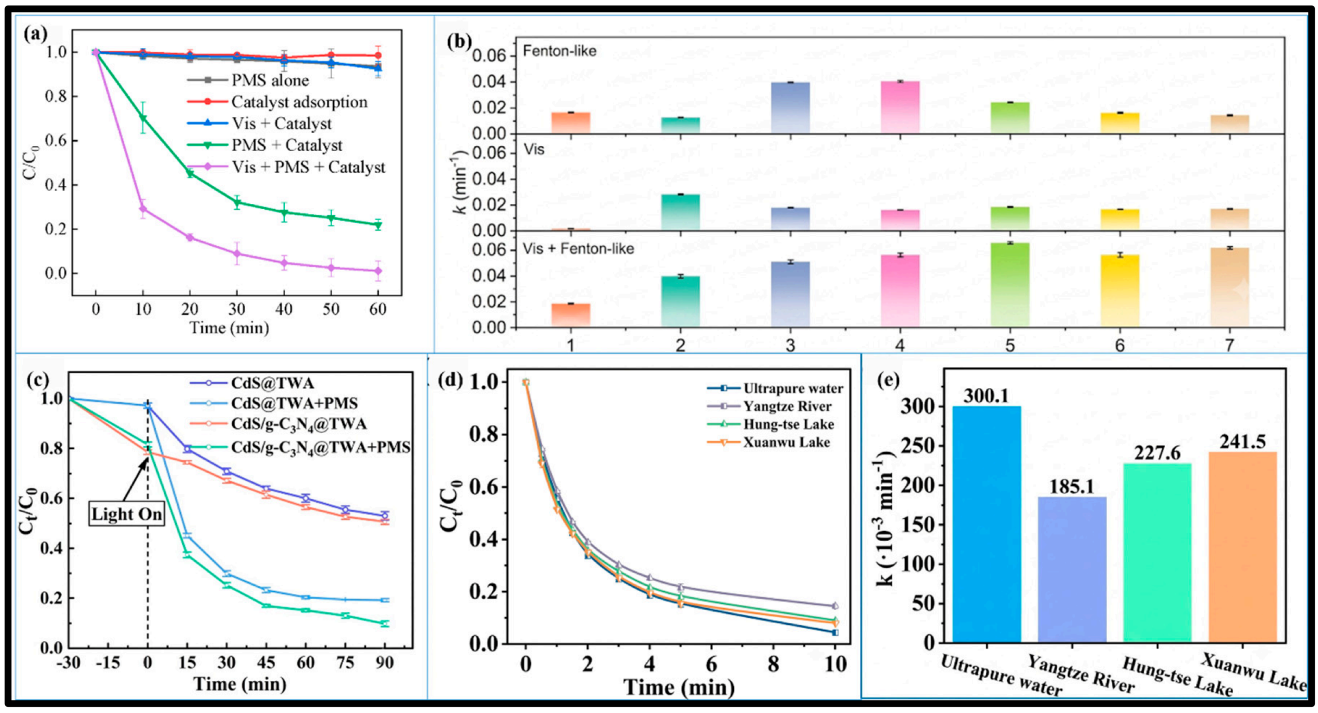



**Figure 9.** g-$C_3N_4$−based PMS-assisted photocatalytic systems for antibiotic degradation: (**a**) synergistic PMS activation by $CuInS_2$/g-$C_3N_4$ for levofloxacin degradation. Reprinted from [113], which is open access and permits unrestricted use of materials under the terms of the creative commons CC-BY. (**b**) Photo−Fenton−like tetracycline degradation over Co/Fevdoped g-$C_3N_4$. Reprinted with permission from [127], Copyright 2023 American Chemical Society. (**c**) Immobilized CdS/g-$C_3N_4$@wood-aerogel system for PMS−driven tetracycline removal. Reprinted with permission from [116], Copyright 2024 American Chemical Society. (**d**,**e**) $Co_3O_4$/g-$C_3N_4$/PMS performance and kinetic stability in ultrapure and real water matrices. Reprinted with permission from [112], Copyright 2025, American Chemical Society.

A similar study was conducted by Shi et al. [127], who investigated Co/Fe bimetal-doped g-$C_3N_4$ to understand the interaction between visible-light photocatalysis and PMS-based Fenton-like oxidation. Figure 9b shows the reaction-rate constants of different systems (1–7) under Fenton-like, visible-light, and combined photo-Fenton-like conditions. The Fenton-like process and the visible-light process alone removed the pollutant at slower rates. However, when both processes were used together, the degradation rate increased significantly. This demonstrate that combining photocatalysis with PMS activation en-

hances the overall oxidation efficiency. Among all the catalysts, the MCN$Co_{2.5}Fe_{2.5}$ sample showed the best photo-Fenton-like performance, suggesting that the appropriate amount of Co and Fe active sites is important for achieving strong synergistic oxidation.

Different from modifying catalyst composition, Zhang et al. [116] reported an immobilized CdS/g-$C_3N_4$ heterojunction constructed on thiolated wood aerogel (TWA) for PMS-assisted tetracycline degradation. As presented in Figure 9c, CdS/g-$C_3N_4$@TWA showed much higher tetracycline removal than CdS@TWA, especially in the presence of PMS, confirming the beneficial role of g-$C_3N_4$ in improving charge transfer and PMS activation. The system achieved 95.32% tetracycline degradation under simulated sunlight. In addition, the wood-aerogel framework provided a three-dimensional support that improved catalyst immobilization and recovery, offering a sustainable strategy for developing reusable photocatalytic systems. Additionally, Wu et al. [112] fabricated a $Co_3O_4$/g-$C_3N_4$ van der Waals heterojunction (CCN-3) for visible-light-assisted PMS activation to degrade tetracycline. As shown in Figure 9d, the CCN-3/PMS system maintained rapid tetracycline removal in ultrapure water as well as in different natural water matrices, including Yangtze River, Hung-tse Lake, and Xuanwu Lake water. The corresponding kinetic analysis in Figure 9e further confirmed that the apparent reaction-rate constants remained high under real-water conditions, demonstrating the strong environmental adaptability of the catalyst. The stable performance was attributed to efficient interfacial charge transfer and effective PMS activation at the $Co_3O_4$/g-$C_3N_4$ interface. However, possible interference from dissolved organic matter and inorganic ions should still be considered for practical wastewater applications.

Overall, these studies demonstrate excellent potential of g-$C_3N_4$-based photocatalysts for PMS-assisted antibiotic degradation. However, direct comparison of the reported degradation efficiencies should be made with caution because the experimental conditions vary considerably among studies. Parameters such as catalyst dosage, PMS concentration, initial antibiotic concentration, solution pH, irradiation source, and reaction time all significantly influence the observed photocatalytic performance. Therefore, degradation efficiency alone may not accurately reflect the intrinsic activity of a photocatalyst, and these operating conditions should be considered when evaluating and comparing different photocatalytic systems.

**Table 2.** Summary of photocatalytic degradation of antibiotics using g-$C_3N_4$-based materials, with emphasis on their role in PMS activation process and associated degradation efficiencies.

| Photocatalyst | Photocatalyst Dosage (g $L^{-1}$) | Synthesis Method | Contaminant (concentration) (mg $L^{-1}$) | Oxidant (concentration) | Bandgap (eV) | Surface Area ($m^2$ $g^{-1}$) | Reaction Conditions | | | Results | | | Reference |
|---|---|---|---|---|---|---|---|---|---|---|---|---|---|
| | | | | | | | Light Source | pH | Time (min) | Degradation (%) | TOC Removal (%) | $k_{obs}$ ($min^{-1}$) | |
| BC/CN | 0.2 | NR | Tetracycline (TC) (10) | PMS (0.2 g $L^{-1}$) | 2.48 | 52.14 | Visible light | 5.45 | 60 | 90 | NR | 0.0355 | [123] |
| FeCu-LDH/g-$C_3N_4$ | 0.1 | Thermal polycondensation and wet-chemical methods | TC (20) | PMS (0.5 mM) | 2.76 | 82.89 | LED lamps | 3.0 | NR | 99 | NR | 0.11539 | [121] |
| B/Mn-co-doped micro-tubular GCN (CNBMn2) | 0.75 | Hydrothermal-assisted co-precipitation | TC (10) | PMS (1.5 mM) | 2.5 | 47 | Xenon lamp (300 W) | 7.0 | 40 | 99 | NR | 0.122 | [124] |
| OCN/Py | 0.16 | Ball-milling-assisted thermal polymerization (or calcination) | TC (10) | PMS 0.5 mM | NR | NR | Visible light | NR | 60 | 97.0 | 97.3 | 0.0568 | [128] |
| $Co_9S_8$/g-$C_3N_4$ | 0.4 | Hydrothermal method | Sulfamethazine (SMR) 20 mg $mL^{-1}$ | PMS (0.8 mM) | 2.51 | NR | Visible light | 7.0 | 40 | 93 | NR | 0.065 | [122] |
| CO-g-$C_3N_4$ | 0.2 | One-step calcination method | Tetracycline hydrochloride (TCH) (10) | PMS (200 mg $L^{-1}$) | 1.91 | 47.97 | Visible light | NR | 60 | 97.77 | 38.26 | 0.07668 | [115] |
| $CoTiO_3$/g-g-$C_3N_4$ | 1.0 | Ultrasonication and calcination method | TCH (10) | PMS (0.2 g $L^{-1}$) | 2.92 | 78.5 | Visible light | 8.0 | 20 | 100 | NR | $3.18 \times 10^{-2}$ | [129] |
| GCN-2.4 | 0.02 | Hydrothermal method | Levofloxacin (LVFX) (10) | PMS (0.2 mM) | NR | 803.76 | NR | 8.9 | 15 | 100 | NR | 0.245 | [130] |
| CuS/g-$C_3N_4$ | 0.1 | simple precipitation method | TC (20) | PMS (0.5 mM) | 1.88 | 27.07 | Visible light | 7.0 | 30 | 97.46 | 58.65 | 0.0051 | [131] |
| $Co_3O_4$-g-$C_3N_4$ | 0.5 | Calcination method | Moxifloxacin (MOX) (20) | PMS (0.5 mM) | NR | 97.22 | NR | 6.3 | 21 | 100 | 69.57 | 0.1858 | [132] |
| CA/FNCCN | 0.8 | Thermal polymerization method | Sulfamethoxazole (SMX) (5.0) | PMS (0.5 g $L^{-1}$) | NR | NR | Visible light | NR | 40 | 99.18 | NR | 0.0951 | [133] |
| $BiVO_4$/g-$C_3N_4$ (BVO/CN) | 0.4 | Ultrasound-assisted dispersion technique | LVFX (20) | PMS (1.0 mM) | 2.47 | 27.41 | Visible light | 6.9 | 40 | 97.7 | 83.3 | NR | [134] |
| FeOOH/HCN-2 | 0.1 | In situ precipitation method | Doxycycline hydrochloride (DXC) (20) | PMS (0.10 mM) | NR | NR | visible light | NR | 30 | 82.2 | NR | 0.0542 | [126] |
| Fe, N-CQDs/g-$C_3N_4$ FNCNN | 0.4 | Fe–N bridge by hydrothermal and thermal polymerization | SMX (5.0) | PMS (0.5 g $L^{-1}$) | 2.18 | 84.59 | Visible light | 6.0 | 40 | 98.61 | 40.58 | 0.0963 | [135] |
| Co/Fe-CN | 0.4 | Facile thermal polymerization | LVFX (20) | PMS (1.0 mM) | 2.84 | 55.76 | Visible light | 6.8 | 50 | 92.1 | 71.3 | 0.638 | [120] |
| $CeO_2$/g-$C_3N_4$ | 1.0 | One-step calcination method | TC (10) | PMS (0.3 mmol/L) | NR | 18.06 | LED lamp (12 W) | NR | 50 | 81.85 | NR | NR | [136] |
| $Fe_3O_4$-$ZnLn_2S_4$ | 0.4 | Solvothermal method | Sulfadiazine (SDZ) (10) | PMS (2.0 mM) | 1.92 | 350 | Xenon lamp (300 W) | 3.0 | 60 | 97.54 | 68.06 | $5.64 \times 10^{-2}$ | [137] |
| 3NiO/g-$C_3N_4$ | 0.2 | Calcination | Tetracycline (20) | PMS (0.1 g $L^{-1}$) | NR | 85.07 | Visible light | 5.0 | 60 | 100 | 63.2 | 0.08032 | [138] |
| Co/g-$C_3N_4$ | 0.1 | Thermal polymerization | CIP (10) | PMS (0.6 mM) | 2.60 | 14.94 | Xenon lamp (350 W) | 7.0 | 150 | 88.87 | NR | NR | [114] |
| Co-doped g-$C_3N_4$ | 0.2 | Hydrothermal and high-temperature calcination methods | TC (20) | PMS (1.0 mM) | 2.26 | NR | Visible light | NR | 20 | 95.9 | NR | 0.1354 | [139] |

Note: In this table, NR stands for not reported.

## 5. Factors Affecting the Photocatalytic Degradation Process

The efficiency of photocatalytic degradation process is strongly influenced by various operational parameters. Variations in these factors can significantly influence the generation of reactive species, pollutant adsorption, and overall degradation performance. Therefore, understanding and optimizing these parameters are essential for achieving efficient photocatalytic treatment. The major factors influencing photocatalytic degradation are discussed below.

### *5.1. Photocatalyst Dosage*

Photocatalyst dosage is a key operational parameter that significantly affects the efficiency of photocatalytic degradation process. In general, increasing the amount of photocatalyst enhances degradation efficiency because more catalyst particles provide a larger number of active sites for pollutant adsorption and degradation reactions. A higher photocatalyst loading also enhances photon absorption, promoting electron excitation from the valence band (VB) to the conduction band (CB) and facilitating the separation of photogenerated electron-hole pairs, which subsequently participate in the generation of reactive oxygen species (ROS) responsible for pollutant degradation. However, increasing the amount of photocatalyst beyond the optimum level may adversely affect photocatalytic activity. An excessive amount of photocatalyst leads to particle agglomeration and enhanced light scattering, which reduce light penetration and limits the activation of photocatalyst particles. Consequently, the overall degradation efficiency decreases. Therefore, proper optimization of photocatalyst loading is necessary to maintain a balance between the availability of sufficient active sites and efficient light utilization, thereby achieving maximum photocatalytic activity [55]. Many researchers have investigated the effects of photocatalyst dosage on the degradation efficiency. For example, Ruiz-Santoyo et al. [140] reported that increasing the amount of g-$C_3N_4$-$Bi_2O_3$ photocatalyst from 100 to 300 mg enhanced the degradation efficiency of tetracycline hydrochloride from 85 to 97% after 90 min of light irradiation. This enhancement was attributed to the increased availability of active sites for pollutant adsorption and degradation.

Similarly, Ahmad et al. [141] studied the photocatalytic degradation of carbamazepine (CBZ) using a $TiO_2$/CdS photocatalyst. They reported increase in removal efficiency from 59.21 to 87.44% with increasing photocatalyst dosage from 0.1 to 0.5 g $L^{-1}$. However, further increasing the dosage to 0.7 g $L^{-1}$ led to a decrease in efficiency to 79.30%, which was attributed to excessive photocatalyst loading, causing higher turbidity and light scattering in solution, thereby reducing light penetration and the number of active sites effectively activated.

### *5.2. Solution pH*

Solution pH is an important parameter in photocatalytic degradation processes as it strongly affects the reaction rate through several mechanisms. The pH controls the surface charge of the photocatalyst, which directly affects the adsorption behavior of pollutant molecules. In general, the photocatalyst surface becomes positively charged under acidic conditions and negatively charged under alkaline conditions. The influence of pH is mainly associated with photocatalytic oxidation by photogenerated holes ($h^+$), the activity of $^{\bullet}OH$, and the reduction process involving conduction band electrons [142]. According to Zyoud et al. this behavior can be explained in terms of the point of zero charge (PZC), defined as the pH at which the photocatalyst surface carries no net charge [143]. The photocatalyst surface becomes positively charged below the PZC and negatively charged above PZC. This variation in surface charge directly affects pollutant adsorption. For cationic pollutants, adsorption decreases below the PZC due to electrostatic repulsion,

while it increases above the PZC because of electrostatic attraction to the negatively charged surface. In contrast, anionic pollutants show better adsorption under acidic conditions, where the positively charged surface enhances attraction. Therefore, precise control of the reaction pH is essential, as it modulates the surface properties of the photocatalyst and governs its interactions with different pollutants, ultimately determining the photocatalytic efficiency [144].

In PMS-assisted photocatalytic systems, solution pH also influences PMS activation and ROS generation. Mildly acidic to near-neutral conditions generally favor the formation of $SO_4^{\bullet-}$ and $^{\bullet}OH$, resulting in enhanced pollutant degradation. In contrast, alkaline conditions promote the conversion of $SO_4^{\bullet-}$ to $^{\bullet}OH$ and accelerate PMS self-decomposition, thereby reducing oxidation efficiency. Therefore, the optimum pH depends on the photocatalyst, target pollutant, and reaction conditions [114]. For instance, Guo et al. [120] investigated the effect of solution pH on the degradation of levofloxacin using a Co/Fe-CN/PMS/visible-light system. The degradation efficiency increased from 83.7% at pH 3 to 92.1% at near-neutral pH (6.8), but decreased to 84.5% and 69.7% at pH 9 and 11, respectively. The enhanced performance under near-neutral conditions was attributed to more efficient PMS activation and ROS generation, whereas alkaline conditions promoted the conversion of $SO_4^{\bullet-}$ to the less selective $^{\bullet}OH$ and accelerated PMS self-decomposition, thereby reducing oxidation efficiency.

### *5.3. Temperature*

An increase in temperature generally enhances the efficiency of photocatalytic processes. High temperature promotes pollutant degradation and enhances reaction kinetics which is possibly due to its role in facilitating the generation of free radicals and helps in reducing electron–hole ($e^-$-$h^+$) recombination, leading to the effective degradation of organic pollutants on the catalyst surface [56]. Numerous studies have demonstrated the effect of temperature on photocatalytic performance. For example, Wang et al. [145] reported that elevated temperature enhanced the degradation of polyethylene, polypropylene, and polystyrene. Soares et al. suggested that the optimal temperature range for photocatalytic reactions is 40–50 °C. At lower temperatures, the reaction may be limited by slow desorption of products from the catalyst surface relative to reactant adsorption and surface degradation. As the temperature increases, the rate-controlling step shifts toward pollutant adsorption on the catalyst surface. However, temperatures above 80 °C can significantly increase charge carrier recombination, leading to reduced photocatalytic efficiency. Therefore, maintaining the reaction temperature within range of 20–80 °C is essential for effective photocatalytic degradation [56].

### *5.4. Pollutant Concentration*

Pollutant concentration is a key factor affecting photocatalytic degradation efficiency. Numerous studies have shown that the degradation rate depends strongly on the initial concentration of the pollutant. In photocatalytic systems, the adsorption of pollutant molecules on the catalyst surface is an important step because it determines their interactions with ROS such as $^{\bullet}OH$ and $O_2^{\bullet-}$. At lower pollutant concentrations, sufficient active sites are available on the photocatalyst surface, allowing efficient adsorption and rapid degradation. However, as pollutant concentrations increase, a larger number of molecules compete for limited active sites, leading to surface saturation and reduced degradation performance. In addition, high pollutant concentrations can hinder light penetration into the reaction medium, thereby decreasing photon absorption by the photocatalyst and limiting ROS generation. The chemical structure and stability of pollutants also influence their susceptibility to photocatalytic oxidation, as different compounds exhibit different

reactivity [146]. Anwar et al. [147] reported atrazine (ATZ) degradation using an N-GO photocatalyst and found that lower pollutant concentrations resulted in higher removal efficiency. About 99.5% degradation was achieved at 5 mg $L^{-1}$ after 90 min of visible-light irradiation, whereas the degradation efficiency decreased to 94.4 and 69.8% at 10 and 15 mg $L^{-1}$, respectively. This decline in degradation efficiency at higher ATZ concentrations was attributed to active site saturation and increased competition between pollutant molecules and intermediates for reactive oxygen species. Furthermore, at ATZ concentrations of 5, 10, and 15 mg $L^{-1}$, the corresponding observed rate constants were 0.0548, 0.0338, and 0.0095 $min^{-1}$, respectively, indicating a decrease in photocatalytic degradation kinetics with increasing pollutant concentrations. Similarly, Gao et al. [148] studied tetracycline (TC) degradation using g-$C_3N_4$/stilbite under visible-light irradiation and observed that increasing TC concentration negatively affected the photocatalytic activity because of active site blockage and reduced light absorption by the catalyst.

### *5.5. Light Intensity and Wavelength*

Photocatalytic degradation of pollutants is strongly influenced by both light intensity and wavelength because these parameters directly affect the excitation of electrons within the photocatalyst. Upon absorbing photons with sufficient energy, electrons are excited from the VB to the CB, generating electron–hole pairs that facilitate ROS formation and pollutant degradation. Generally, the photocatalytic reaction rate increases with light intensity and initially follows a linear relationship. However, at higher light intensities, the reaction rate often shifts to a square-root dependence due to enhanced electron–hole recombination. In most photocatalytic systems, visible-light irradiation is widely used to drive pollutant degradation. Several studies have demonstrated a strong correlation between light intensity and degradation efficiency. It has also been reported that increasing the light intensity above 600 lux can significantly reduce the irradiation time required for effective pollutant degradation [149].

## 6. Conclusions and Future Perspectives

This review highlights the significant potential of g-$C_3N_4$-based materials for PMS-assisted visible light photocatalytic degradation of antibiotic pollutants. Owing to their suitable band structure, visible-light responsiveness, low toxicity, environmental compatibility, and cost-effective synthesis, g-$C_3N_4$-based materials have emerged as promising photocatalysts for sustainable water treatment applications. Various synthesis approaches for g-$C_3N_4$-based photocatalysts, including hydrothermal, solvothermal, microwave-assisted, calcination, sol–gel, and green synthesis methods, have been discussed. Furthermore, the integration of peroxymonosulfate (PMS) with g-$C_3N_4$-based photocatalysts has accelerated antibiotic degradation through the generation of reactive oxygen species (ROS), such as $SO_4^{\bullet-}$, $^{\bullet}OH$, and $O_2^{\bullet-}$, under visible-light irradiation. This review also emphasizes that operational parameters, such as photocatalyst dosage, solution pH, reaction temperature, pollutant concentration, and light intensity, strongly influence photocatalytic degradation efficiency. Therefore, careful optimization of these parameters is essential for achieving stable, efficient, and practically applicable photocatalytic systems. Overall, this review underscores the crucial role of g-$C_3N_4$-based photocatalytic systems in the degradation of antibiotic pollutants, thereby contributing to the advancement of sustainable environmental remediation technologies. Future research should focus on improving the long-term stability, scalability, and practical applicability of g-$C_3N_4$-based photocatalytic systems, while further elucidating PMS activation mechanisms and evaluating their performance under real environmental conditions.

Despite the remarkable progress achieved in recent years, several challenges still hinder the practical applications of g-$C_3N_4$-based photocatalytic systems. These limitations include rapid electron–hole recombination, insufficient visible light utilization, catalyst deactivation during long-term operation, and reduced photocatalytic efficiency in real wastewater systems. Moreover, the formation of degradation intermediates, incomplete mineralization of pollutants, and the influence of coexisting ions remain important concerns that require further investigation.

Catalytic stability remains a critical challenge for the practical application of g-$C_3N_4$-based PMS-assisted photocatalytic systems. During prolonged use, photocatalytic activity may gradually decrease due to surface fouling, blockage of active sites, structural changes, or reduced charge-transfer efficiency. Therefore, future studies should carefully evaluate catalyst performance over repeated cycles and long-term operation. Stability may be improved through heterojunction engineering, stronger interfacial coupling, defect control, surface modification, and suitable regeneration methods.

Recovery and reuse of slurry-based dispersed photocatalysts is another important practical issue. Although slurry systems provide good contact between catalysts, PMS, light, and pollutants, separation of fine catalyst particles after treatment can be difficult and may increase operational cost. Therefore, immobilization of g-$C_3N_4$-based photocatalysts on suitable supports should be further explored. Possible approaches include thin-film catalysts, membrane-supported catalysts, coated substrates, magnetic composites, and monolithic structures. These strategies may improve catalyst handling, recovery, reuse, and suitability for continuous wastewater treatment.

In addition to catalyst stability and recovery, several practical challenges still restrict the real-world application of g-$C_3N_4$-based PMS-assisted photocatalytic systems for antibiotic-contaminated wastewater. These include reduced efficiency in complex wastewater matrices, interference from coexisting ions and natural organic matter, incomplete mineralization, possible toxicity of degradation intermediates, difficulty in maintaining long-term photocatalytic performance, and scale-up limitations. Therefore, future research should move beyond ideal laboratory conditions and focus on real wastewater testing, toxicity evaluation, mineralization efficiency, continuous-flow reactor design, and reusable catalyst configurations.

To address these challenges, future research should focus on the following aspects:

- Develop low-cost, scalable, and environmentally sustainable synthesis methods using abundant and inexpensive precursors.
- Rationally design g-$C_3N_4$-based photocatalysts through precise control of their structural and electronic properties to enhance photocatalytic performance.
- Significant efforts are required to broaden the light absorption range of g-$C_3N_4$-based photocatalysts. Researchers should focus on developing novel materials and structural designs, such as hybrid systems combined with semiconductors, to enhance visible-light absorption and improve photocatalytic performance.
- Comprehensively identified degradation pathways and toxicity assessment of intermediate products using suitable biological assays to ensure complete mineralization and the environmental safety.
- Improve catalyst durability, recyclability, and long-term operational stability through systematic evaluation over multiple reuse cycles. Future studies should also investigate catalyst deactivation mechanisms, including photocorrosion, active-site loss, structural degradation, and possible metal leaching in modified g-$C_3N_4$-based photocatalysts.
- Focus on the large-scale production and practical implementation of g-$C_3N_4$-based photocatalysts, supported by techno-economic analysis and life-cycle assessment, to

evaluate synthesis costs, PMS consumption, energy requirements, catalyst recovery, operational feasibility, and environmental impacts.

- Develop efficient photocatalyst recovery strategies, such as immobilized photocatalysts, membrane-supported systems, magnetic photocatalysts, and self-supporting photoelectrodes, to facilitate catalyst separation, minimize material loss, and improve long-term operational stability.
- Evaluate photocatalytic performance in real wastewater matrices containing natural organic matter, inorganic ions, and coexisting contaminants to better assess catalyst performance under practical environmental conditions.
- Utilize computational modeling and mathematical simulations effectively predict the properties and photocatalytic performance of g-$C_3N_4$-based materials. This approach can facilitate the optimization of synthesis strategies while reducing the need for complex and time-consuming experimental trials.

Addressing these challenges will contribute to the development of stable, scalable, and highly efficient g-$C_3N_4$-based photocatalytic systems, thereby promoting their real-world application for sustainable antibiotic remediation in aquatic environments.

**Author Contributions:** W.U.: Conceptualization, Data curation, Investigation, Methodology, Visualization, Writing—original draft. F.A.: Methodology, Validation, Writing—original draft. S.I.A.S.: Investigation, Visualization, Resources, Writing—original draft. M.A. (Muhammad Anwar): Methodology, Resources, Software, Writing—original draft. S.A.: Resources, Visualization, Writing—review and editing. M.A. (Muhammad Ateeq): Resources, Validation, Supervision, Writing—review and editing. N.S.S.: Validation, Visualization, Writing—review and editing. J.A.K.: Conceptualization, Project administration, Supervision, Validation, Funding acquisition, Writing—review and editing. C.H.: Conceptualization, Funding acquisition, Validation, Resources, Writing—review and editing. All authors have read and agreed to the published version of the manuscript.

**Funding:** The Higher Education Commission (HEC), Pakistan, is highly acknowledged for financial support through the National Research Program for Universities (NRPU) Project, Ref No. 20-15851/NRPU/R&D/HEC/2021-2020. CH also acknowledged the support by the National Research Foundation of Korea (NRF) grant funded by the Korean government (MSIT) (No. RS-2025-00461931) and the support of the "Cooperative Research Program for Agriculture Science and Technology Development (Project No. RS-2026-25504096)" Rural Development Administration, Republic of Korea.

**Data Availability Statement:** No new data were created or analyzed in this study. Data sharing is not applicable to this article.

**Conflicts of Interest:** The authors declare no conflicts of interest.

## References

1. Yang, D.; Yang, Y.; Xia, J. Hydrological cycle and water resources in a changing world: A review. *Geogr. Sustain.* **2021**, *2*, 115–122. [CrossRef]
2. Kaminski, W.; Marszalek, J.; Tomczak, E. Water desalination by pervaporation—Comparison of energy consumption. *Desalination* **2018**, *433*, 89–93. [CrossRef]
3. Shah, S.I.A.; Ahmad, W.; Anwar, M.; Shah, R.; Khan, J.A.; Shah, N.S.; Al-Anazi, A.; Han, C. Synthesis, properties, and applications of $Fe_3O_4$ and $Fe_3O_4$-based nanocomposites: A review. *Appl. Catal. O Open* **2025**, *203*, 207049. [CrossRef]
4. Karimian, H.; Li, Y.; Chen, Y.; Wang, Z. Evaluation of different machine learning approaches and aerosol optical depth in $PM_{2.5}$ prediction. *Environ. Res.* **2023**, *216*, 114465. [CrossRef] [PubMed]
5. Sanda, B.Y.; Ibrahim, I. Causes, categories and control of water pollution. *Int. J. Sci. Eng. Sci.* **2020**, *4*, 84–90.
6. Saravanan, A.; Kumar, P.S.; Hemavathy, R.; Jeevanantham, S.; Harikumar, P.; Priyanka, G.; Devakirubai, D.R.A. A comprehensive review on sources, analysis and toxicity of environmental pollutants and its removal methods from water environment. *Sci. Total Environ.* **2022**, *812*, 152456. [CrossRef] [PubMed]

7. Chinnasamy, C.; Perumal, N.; Choubey, A.; Rajendran, S. Recent advancements in MXene-based nanocomposites as photocatalysts for hazardous pollutant degradation—A review. *Environ. Res.* **2023**, *233*, 116459. [CrossRef] [PubMed]
8. Dutt, M.A.; Hanif, M.A.; Nadeem, F.; Bhatti, H.N. A review of advances in engineered composite materials popular for wastewater treatment. *J. Environ. Chem. Eng.* **2020**, *8*, 104073. [CrossRef]
9. Tariq, A.; Mushtaq, A. Untreated wastewater reasons and causes: A review of most affected areas and cities. *Int. J. Chem. Biochem. Sci.* **2023**, *23*, 121–143.
10. Javaid, A.; Latif, S.; Imran, M.; Hussain, N.; Bilal, M.; Iqbal, H.M.N. MXene-based hybrid composites as photocatalyst for the mitigation of pharmaceuticals. *Chemosphere* **2022**, *291*, 133062. [CrossRef] [PubMed]
11. Marinho, B.A.; Suhadolnik, L.; Likozar, B.; Huš, M.; Marinko, Ž.; Čeh, M. Photocatalytic, electrocatalytic and photoelectrocatalytic degradation of pharmaceuticals in aqueous media: Analytical methods, mechanisms, simulations, catalysts and reactors. *J. Clean. Prod.* **2022**, *343*, 131061. [CrossRef]
12. Ali, F.; Khan, J.A.; Shah, N.S.; Sayed, M.; Khan, H.M. Carbamazepine degradation by UV and UV-assisted AOPs: Kinetics, mechanism and toxicity investigations. *Process Saf. Environ. Prot.* **2018**, *117*, 307–314. [CrossRef]
13. Ortúzar, M.; Esterhuizen, M.; Olicón-Hernández, D.R.; González-López, J.; Aranda, E. Pharmaceutical Pollution in Aquatic Environments: A Concise Review of Environmental Impacts and Bioremediation Systems. *Front. Microbiol.* **2022**, *13*, 869332. [CrossRef] [PubMed]
14. Dung Nguyen, M.; Binh Nguyen, T.; Hai Tran, L.; Giang Nguyen, T.; Fatimah, I.; Prasetyo Kuncoro, E.; Doong, R.-A. Z-scheme S, B co-doped g-$C_3N_4$ nanotube@$MnO_2$ heterojunction with visible-light-responsive for enhanced photodegradation of diclofenac by peroxymonosulfate activation. *Chem. Eng. J.* **2023**, *452*, 139249. [CrossRef]
15. González-Poggini, S.; Rosenkranz, A.; Colet-Lagrille, M. Two-Dimensional Nanomaterials for the Removal of Pharmaceuticals from Wastewater: A Critical Review. *Processes* **2021**, *9*, 2160. [CrossRef]
16. Hejna, M.; Kapuścińska, D.; Aksmann, A. Pharmaceuticals in the Aquatic Environment: A Review on Eco-Toxicology and the Remediation Potential of Algae. *Int. J. Environ. Res. Public Health* **2022**, *19*, 7717. [CrossRef] [PubMed]
17. Waleng, N.J.; Nomngongo, P.N. Occurrence of pharmaceuticals in the environmental waters: African and Asian perspectives. *Environ. Chem. Ecotoxicol.* **2022**, *4*, 50–66. [CrossRef]
18. Chang, C.-T.; Wang, J.-J.; Ouyang, T.; Zhang, Q.; Jing, Y.-H. Photocatalytic degradation of acetaminophen in aqueous solutions by $TiO_2$/ZSM-5 zeolite with low energy irradiation. *Mater. Sci. Eng. B* **2015**, *196*, 53–60. [CrossRef]
19. Menz, J.; Toolaram, A.P.; Rastogi, T.; Leder, C.; Olsson, O.; Kümmerer, K.; Schneider, M. Transformation products in the water cycle and the unsolved problem of their proactive assessment: A combined in vitro/in silico approach. *Environ. Int.* **2017**, *98*, 171–180. [CrossRef] [PubMed]
20. Thakur, R.; Singh, A.; Dhanwar, R.; Kadam, S.; Waghmare, U.; Lodha, T.; Lopes, B.S.; Prakash, O. Global perspectives on residual antibiotics: Environmental challenges and trends. *Discov. Sustain.* **2025**, *6*, 232. [CrossRef]
21. Mutuku, C.; Gazdag, Z.; Melegh, S. Occurrence of antibiotics and bacterial resistance genes in wastewater: Resistance mechanisms and antimicrobial resistance control approaches. *World J. Microbiol. Biotechnol.* **2022**, *38*, 152. [CrossRef] [PubMed]
22. Parsa, J.B.; Panah, T.M.; Chianeh, F.N. Removal of ciprofloxacin from aqueous solution by a continuous flow electro-coagulation process. *Korean J. Chem. Eng.* **2016**, *33*, 893–901. [CrossRef]
23. Zhou, J.; Yun, X.; Wang, J.; Li, Q.; Wang, Y. A review on the ecotoxicological effect of sulphonamides on aquatic organisms. *Toxicol. Rep.* **2022**, *9*, 534–540. [CrossRef] [PubMed]
24. Batt, A.L.; Bruce, I.B.; Aga, D.S. Evaluating the vulnerability of surface waters to antibiotic contamination from varying wastewater treatment plant discharges. *Environ. Pollut.* **2006**, *142*, 295–302. [CrossRef] [PubMed]
25. Danner, M.-C.; Robertson, A.; Behrends, V.; Reiss, J. Antibiotic pollution in surface fresh waters: Occurrence and effects. *Sci. Total Environ.* **2019**, *664*, 793–804. [CrossRef] [PubMed]
26. Wang, J.; Zhuan, R. Degradation of antibiotics by advanced oxidation processes: An overview. *Sci. Total Environ.* **2020**, *701*, 135023. [CrossRef] [PubMed]
27. Jin, J.; Xu, L.; Zhang, S.; Jin, M.; Zhang, P.; Shen, L.; Chen, J.; Li, Z.; Zhao, W.; Liu, H. Oxidative response of rice (*Oryza sativa* L.) seedlings to quinolone antibiotics and its correlation with phyllosphere microbes and antibiotic resistance genes. *Sci. Total. Environ.* **2023**, *867*, 161544. [CrossRef] [PubMed]
28. Pietropoli, E.; Zgheib, R.; Selmo, M.; Melotto, G.; Lopparelli, R.M.; Lucatello, L.; Pauletto, M.; De Liguoro, M. Aquatic Toxicity of Antibiotics Ciprofloxacin and Sulfamethoxazole: Significant Impact on Early Life Stages of Crustaceans, a Marine Diatom, and a Freshwater Plant. *Toxics* **2025**, *13*, 979. [CrossRef] [PubMed]
29. Kovalakova, P.; Cizmas, L.; McDonald, T.J.; Marsalek, B.; Feng, M.; Sharma, V.K. Occurrence and toxicity of antibiotics in the aquatic environment: A review. *Chemosphere* **2020**, *251*, 126351. [CrossRef] [PubMed]
30. Adebisi, Y.A.; Ogunkola, I.O. The global antimicrobial resistance response effort must not exclude marginalised populations. *Trop. Med. Health* **2023**, *51*, 33. [CrossRef] [PubMed]

31. Fernández, A.M.L.; Rendueles, M.; Díaz, M. Sulfamethoxazole Removal from Synthetic Solutions by Ion Exchange using a Strong Anionic Resin in Fixed Bed. *Solvent Extr. Ion Exch.* **2013**, *31*, 763–781. [CrossRef]
32. Herraiz-Carboné, M.; Cotillas, S.; Lacasa, E.; Sainz de Baranda, C.; Riquelme, E.; Cañizares, P.; Rodrigo, M.A.; Sáez, C. A review on disinfection technologies for controlling the antibiotic resistance spread. *Sci. Total Environ.* **2021**, *797*, 149150. [CrossRef] [PubMed]
33. Roslan, N.N.; Lau, H.L.H.; Suhaimi, N.A.A.; Shahri, N.N.M.; Verinda, S.B.; Nur, M.; Lim, J.-W.; Usman, A. Recent Advances in Advanced Oxidation Processes for Degrading Pharmaceuticals in Wastewater—A Review. *Catalysts* **2024**, *14*, 189. [CrossRef]
34. Mukherjee, J.; Lodh, B.K.; Sharma, R.; Mahata, N.; Shah, M.P.; Mandal, S.; Ghanta, S.; Bhunia, B. Advanced oxidation process for the treatment of industrial wastewater: A review on strategies, mechanisms, bottlenecks and prospects. *Chemosphere* **2023**, *345*, 140473. [CrossRef] [PubMed]
35. Pandis, P.K.; Kalogirou, C.; Kanellou, E.; Vaitsis, C.; Savvidou, M.G.; Sourkouni, G.; Zorpas, A.A.; Argirusis, C. Key Points of Advanced Oxidation Processes (AOPs) for Wastewater, Organic Pollutants and Pharmaceutical Waste Treatment: A Mini Review. *ChemEngineering* **2022**, *6*, 8. [CrossRef]
36. Truong, H.B.; Bae, S.; Cho, J.; Hur, J. Advances in application of g–C3N4–based materials for treatment of polluted water and wastewater via activation of oxidants and photoelectrocatalysis: A comprehensive review. *Chemosphere* **2022**, *286*, 131737. [CrossRef] [PubMed]
37. Hasija, V.; Nguyen, V.-H.; Kumar, A.; Raizada, P.; Krishnan, V.; Khan, A.A.P.; Singh, P.; Lichtfouse, E.; Wang, C.; Thi Huong, P. Advanced activation of persulfate by polymeric g-$C_3N_4$ based photocatalysts for environmental remediation: A review. *J. Hazard. Mater.* **2021**, *413*, 125324. [CrossRef] [PubMed]
38. Chakravorty, A.; Roy, S. A review of photocatalysis, basic principles, processes, and materials. *Sustain. Chem. Environ.* **2024**, *8*, 100155. [CrossRef]
39. Solangi, N.H.; Karri, R.R.; Mazari, S.A.; Mubarak, N.M.; Jatoi, A.S.; Malafaia, G.; Azad, A.K. MXene as emerging material for photocatalytic degradation of environmental pollutants. *Coord. Chem. Rev.* **2023**, *477*, 214965. [CrossRef]
40. Wen, J.; Xie, J.; Chen, X.; Li, X. A review on g-$C_3N_4$-based photocatalysts. *Appl. Surf. Sci.* **2017**, *391*, 72–123. [CrossRef]
41. Murali, A.; Sunil, S.; Free, M.; Sarswat, P. Enhanced interfacial charge transfer by Z-scheme in defect-mediated ZnO-CdS nano-composite with rGO as a solid-state electron mediator for efficient photocatalytic applications. *arXiv* **2023**, arXiv:2308.05211. [CrossRef]
42. Javed, M.; Qamar, M.A.; Shahid, S.; Alsaab, H.O.; Asif, S. Highly efficient visible light active Cu–ZnO/S-g-$C_3N_4$ nanocomposites for efficient photocatalytic degradation of organic pollutants. *RSC Adv.* **2021**, *11*, 37254–37267. [CrossRef] [PubMed]
43. Fu, Y.; Gao, X.; Geng, J.; Li, S.; Wu, G.; Ren, H. Degradation of three nonsteroidal anti-inflammatory drugs by UV/persulfate: Degradation mechanisms, efficiency in effluents disposal. *Chem. Eng. J.* **2019**, *356*, 1032–1041. [CrossRef]
44. Surana, M.; Pattanayak, D.S.; Singh, V.K.; Pal, D. g-$C_3N_4$ based Z-scheme photocatalysts for tetracycline degradation: A comprehensive review. *J. Hazard. Mater. Lett.* **2024**, *5*, 100116. [CrossRef]
45. Humayun, M.; Ullah, H.; Cao, J.; Pi, W.; Yuan, Y.; Ali, S.; Tahir, A.A.; Yue, P.; Khan, A.; Zheng, Z.; et al. Experimental and DFT Studies of Au Deposition Over $WO_3$/g-$C_3N_4$ Z-Scheme Heterojunction. *Nano-Micro Lett.* **2019**, *12*, 7. [CrossRef] [PubMed]
46. Rahman, S.U.; Khan, S.; Ahmad, S.; Shah, S.I.A.; Ali, Z.; Azizi, S.; Maaza, M. Synthesis, Properties, and Photocatalytic Hydrogen Production of G-$C_3N_4$/MXene Composites: A Review. *CLEAN—Soil Air Water* **2026**, *54*, e70114. [CrossRef]
47. Jourshabani, M.; Lee, B.-K.; Shariatinia, Z. From Traditional Strategies to Z-scheme Configuration in Graphitic Carbon Nitride Photocatalysts: Recent Progress and Future Challenges. *Appl. Catal. B* **2020**, *276*, 119157. [CrossRef]
48. Pattanayak, D.S.; Pal, D.; Mishra, J.; Thakur, C.; Wasewar, K.L. Doped graphitic carbon nitride (g-$C_3N_4$) catalysts for efficient photodegradation of tetracycline antibiotics in aquatic environments. *Environ. Sci. Pollut. Res. Int.* **2023**, *30*, 24919–24926. [PubMed]
49. Wang, F.; Feng, Y.; Chen, P.; Wang, Y.; Su, Y.; Zhang, Q.; Zeng, Y.; Xie, Z.; Liu, H.; Liu, Y.; et al. Photocatalytic degradation of fluoroquinolone antibiotics using ordered mesoporous g-$C_3N_4$ under simulated sunlight irradiation: Kinetics, mechanism, and antibacterial activity elimination. *Appl. Catal. B Environ.* **2018**, *227*, 114–122. [CrossRef]
50. Rahman, S.U.; Anwar, S.; Noor, A.; Qayyum, S.; Madeniyet, Y.; Muhammad, N. Engineering MXene-based platforms for electrocatalytic $CO_2$ and $N_2$ reduction reactions; synthesis, modification strategies, and mechanistic insights. *J. Environ. Chem. Eng.* **2026**, *14*, 123689. [CrossRef]
51. Han, X.; Li, M.; Ma, Y.; Li, Y.; Ma, H.; Wang, C. Thermal coupled photocatalysis to enhance $CO_2$ reduction activities on Ag loaded g-$C_3N_4$ catalysts. *Surf. Interfaces* **2021**, *23*, 101006. [CrossRef]
52. Yu, F.; Zhang, J.; Ren, J.; Chen, H.; Tian, X.; Feng, C.; Li, C.; Zhang, J.; Tang, X.; Hou, X. ZnO@g-C3N4 photocatalyst with switchable carrier transfer mechanism between type-II and S-scheme through S doping. *J. Alloys Compd.* **2024**, *982*, 173756. [CrossRef]
53. Haider, Z.; Archana, R.; Ju, H. Recent Advancements in Photocatalytic Synthesis of Five Membered Nitrogen Heterocycles and Their Derivatives. *Molecules* **2025**, *30*, 3490. [CrossRef] [PubMed]

54. Haider, Z.; Ju, H. Strategies to Boost Photocatalytic Degradation of Emerging Contaminants Using ZnO Heterostructure Photocatalysts. *Appl. Sci.* **2026**, *16*, 5279. [CrossRef]
55. Khan, M.A.; Mutahir, S.; Shaheen, I.; Qunhui, Y.; Bououdina, M.; Humayun, M. Recent advances over the doped g-C3N4 in photocatalysis: A review. *Coord. Chem. Rev.* **2025**, *522*, 216227. [CrossRef]
56. Bineta, I.; Kirmani, O. A review of g-$C_3N_4$-based photocatalysts for antibiotic elimination: Mechanistic insights and operational parameters. *Chin. J. Anal. Chem.* **2026**, *54*, 100626. [CrossRef]
57. Imran, M.; Abdullah, A.Z.; Khan, M.E.; Mohammad, A. A focused review on photocatalytic potential of graphitic carbon nitride (g-$C_3N_4$) based metal oxide-nanostructures for effective remediation of most overused antibiotics. *J. Environ. Manag.* **2025**, *373*, 123759. [CrossRef] [PubMed]
58. Kyriakos, P.; Hristoforou, E.; Belessiotis, G.V. Graphitic Carbon Nitride (g-$C_3N_4$) in Photocatalytic Hydrogen Production: Critical Overview and Recent Advances. *Energies* **2024**, *17*, 3159. [CrossRef]
59. Bhanderi, D.; Lakhani, P.; Modi, C.K. Graphitic carbon nitride (g-$C_3N_4$) as an emerging photocatalyst for sustainable environmental applications: A comprehensive review. *RSC Sustain.* **2024**, *2*, 265–287. [CrossRef]
60. Wang, Y.; He, Y.; Lai, Q.; Fan, M. Review of the progress in preparing nano $TiO_2$: An important environmental engineering material. *J. Environ. Sci.* **2014**, *26*, 2139–2177. [CrossRef] [PubMed]
61. Sasikala, S.P.; Poulin, P.; Aymonier, C. Advances in subcritical hydro-/solvothermal processing of graphene materials. *Adv. Mater.* **2017**, *29*, 1605473. [CrossRef] [PubMed]
62. Belew, A.A.; Assege, M.A. Solvothermal synthesis of metal oxide nanoparticles: A review of applications, challenges, and future perspectives. *Results Chem.* **2025**, *16*, 102438. [CrossRef]
63. Vijayakumar, T.; Benoy, M.; Duraimurugan, J.; Kumar, G.S.; Shkir, M.; Maadeswaran, P.; Kumar, A.S.; Kumar, K.R. Hydrothermal synthesis of CuO/g-$C_3N_4$ nanosheets for visible-light driven photodegradation of methylene blue. *Diam. Relat. Mater.* **2022**, *121*, 108735. [CrossRef]
64. Hao, R.; Wang, G.; Jiang, C.; Tang, H.; Xu, Q. In situ hydrothermal synthesis of g-$C_3N_4$/$TiO_2$ heterojunction photocatalysts with high specific surface area for Rhodamine B degradation. *Appl. Surf. Sci.* **2017**, *411*, 400–410. [CrossRef]
65. Wang, L.; Lu, Y.; Xu, J.; Tao, F.; Liang, P. Solvothermal synthesis of g-$C_3N_4$ nanosheets modified carbon quantum dots for enhanced photocatalytic degradation. *Solid State Sci.* **2023**, *143*, 107271. [CrossRef]
66. Shanaah, H.H.; Allangawi, A.; Ahmed, U.; Idrisov, E.; Ali, N.; Attique, S.; Hanif, M.B.; Mahmood, T.; Iqbal, J.; Younis, A. Cobalt-doped graphitic carbon nitride: A multifunctional material for humidity sensing, electrochemical water splitting and environmental remediation applications. *J. Alloys Compd.* **2024**, *1008*, 176498. [CrossRef]
67. Kumar, P.; Banerjee, D.; Sharma, A. Low-temperature hydrothermal synthesis of graphitic carbon nitrate-zinc oxide hybrid and study of its photo-luminescence property. *Next Mater.* **2026**, *11*, 101771. [CrossRef]
68. Dhanu, M.; Perumal, I. Adsorptive removal of uranium from aqueous solutions using $TiO_2$-diglycolamic acid functionalized graphitic carbon nitride ($TiO_2$@ gCN-HDGA) nanocomposite. *Results Chem.* **2026**, *25*, 103248. [CrossRef]
69. Jabbar Khan, A.; Gao, L.; Numan, A.; Khan, S.; Hussain, I.; Sajjad, M.; Shah, S.S.; Mateen, A.; Zhao, G. Recent advancements in the tailoring of nanomaterials via microwave-assisted synthesis: A comprehensive review. *Crit. Rev. Solid State Mater. Sci.* **2025**, *50*, 515–538. [CrossRef]
70. Plubphon, N.; Thongtem, S.; Phuruangrat, A.; Randorn, C.; Kaowphong, S.; Narksitipan, S.; Thongtem, T. Direct microwave heating synthesis and characterization of highly efficient g-$C_3N_4$ photocatalyst. *Inorg. Chem. Commun.* **2022**, *139*, 109386. [CrossRef]
71. Li, Z.; Wang, W.; Liu, Q.; Zhang, Z.; Fang, X. In-situ microwave-assisted heating synthesis of a high-performance g-$C_3N_4$/carbon nanotubes composite photocatalyst with good contact interfaces. *Mater. Res. Bull.* **2018**, *106*, 152–161. [CrossRef]
72. Xie, H.; Zheng, Y.; Guo, X.; Liu, Y.; Zhang, Z.; Zhao, J.; Zhang, W.; Wang, Y.; Huang, Y. Rapid Microwave Synthesis of Mesoporous Oxygen-Doped g-$C_3N_4$ with Carbon Vacancies for Efficient Photocatalytic $H_2O_2$ Production. *ACS Sustain. Chem. Eng.* **2021**, *9*, 6788–6798. [CrossRef]
73. Yamini, J.; Dhanabal, R.; Gomathi Priya, P.; Induja, M. Microwave driven assembly of g-$C_3N_4$ based $WO_3$ nanocubes for enhanced photocatalysis. *Mater. Chem. Phys.* **2025**, *333*, 130323. [CrossRef]
74. Hoang, L.-A.T.; Nguyen, T.D.; Lee, T. Microwave-Assisted Synthesis of Pd/g-$C_3N_4$ for Enhanced Photocatalytic Degradation of Sulfamethoxazole. *Inorganics* **2025**, *13*, 118. [CrossRef]
75. Zhang, Z.; Li, X.; Chen, H.; Shao, G.; Zhang, R.; Lu, H. Synthesis and properties of Ag/ZnO/g-$C_3N_4$ ternary micro/nano composites by microwave-assisted method. *Mater. Res. Express* **2018**, *5*, 015021. [CrossRef]
76. Matias, M.L.; Reis-Machado, A.S.; Rodrigues, J.; Calmeiro, T.; Deuermeier, J.; Pimentel, A.; Fortunato, E.; Martins, R.; Nunes, D. Microwave synthesis of visible-light-activated g-$C_3N_4$/$TiO_2$ photocatalysts. *Nanomaterials* **2023**, *13*, 1090. [CrossRef] [PubMed]
77. Otitoju, T.A.; Ahmad, A.L.; Ooi, B.S. Superhydrophilic (superwetting) surfaces: A review on fabrication and application. *J. Ind. Eng. Chem.* **2017**, *47*, 19–40. [CrossRef]

78. Prasad, C.; Yang, X.; Liu, Q.; Tang, H.; Rammohan, A.; Zulfiqar, S.; Zyryanov, G.V.; Shah, S. Recent advances in MXenes supported semiconductors based photocatalysts: Properties, synthesis and photocatalytic applications. *J. Ind. Eng. Chem.* **2020**, *85*, 1–33. [CrossRef]
79. Lan, D.; Zhu, H.; Zhang, J.; Xie, C.; Wang, F.; Zheng, Y.; Guo, Z.; Xu, M.; Wu, T. Green One-Pot Synthesis of Mesoporous g-$C_3N_4$ for Promoted Organic Dyes Photodegradation in Wastewater Treatment. *Ind. Eng. Chem. Res.* **2024**, *63*, 3491–3503. [CrossRef]
80. Cao, J.; Qin, C.; Wang, Y.; Zhang, B.; Gong, Y.; Zhang, H.; Sun, G.; Bala, H.; Zhang, Z. Calcination Method Synthesis of $SnO_2$/g-$C_3N_4$ Composites for a High-Performance Ethanol Gas Sensing Application. *Nanomaterials* **2017**, *7*, 98. [CrossRef] [PubMed]
81. Liu, R.; Yang, W.; He, G.; Zheng, W.; Li, M.; Tao, W.; Tian, M. Ag-modified g-$C_3N_4$ prepared by a one-step calcination method for enhanced catalytic efficiency and stability. *ACS Omega* **2020**, *5*, 19615–19624. [CrossRef] [PubMed]
82. Wang, T.; Yang, W.; Chang, L.; Wang, H.; Wu, H.; Cao, J.; Fan, H.; Wang, J.; Liu, H.; Hou, Y.; et al. One-step calcination synthesis of accordion-like MXene-derived $TiO_2$@C coupled with g-$C_3N_4$: Z-scheme heterojunction for enhanced photocatalytic NO removal. *Sep. Purif. Technol.* **2022**, *285*, 120329. [CrossRef]
83. Shin, M.; Sharma, K.P.; Awasthi, G.P.; Gwak, N.; Yu, C. One pot calcination method derived g-$C_3N_4$/$Co_3O_4$ composite for photocatalytic degradation of 4-nitrophenol. *J. Mol. Struct.* **2025**, *1341*, 14246. [CrossRef]
84. Singh, R.; Chauhan, M.; Garg, P.; Sharma, B.; Attri, P.; Sharma, R.K.; Sharma, D.; Chaudhary, G.R. A critical review on visible light active graphitic carbon nitride (g-CN) based photocatalyst for environment remediation application: A sustainable approach. *J. Clean. Prod.* **2023**, *427*, 138855. [CrossRef]
85. Estrada-Movilla, E.; Castillo-Saenz, J.; Valdez-Salas, B.; Ortiz-Pérez, Á.; Beltrán-Partida, E.; Salvador-Carlos, J.; Puello-Polo, E. Challenges and Opportunities for g-$C_3N_4$-Based Heterostructures in the Photodegradation of Environmental Pollutants. *Catalysts* **2025**, *15*, 653. [CrossRef]
86. Singhal, M.; Jangir, S.; Upadhyay, S.; Rajawat, D.S. Advances in graphitic carbon nitride: A comprehensive review of synthesis, properties, applications and recent developments with photoelectrochemical water splitting. *Discov. Chem.* **2024**, *1*, 64. [CrossRef]
87. Panimalar, S.; Uthrakumar, R.; Selvi, E.T.; Gomathy, P.; Inmozhi, C.; Kaviyarasu, K.; Kennedy, J. Studies of $MnO_2$/g-$C_3N_4$ hetrostructure efficient of visible light photocatalyst for pollutants degradation by sol-gel technique. *Surf. Interfaces* **2020**, *20*, 100512. [CrossRef]
88. Kumar, A.; Khan, M.; Zeng, X.; Lo, I.M.C. Development of g-$C_3N_4$/$TiO_2$/$Fe_3O_4$@$SiO_2$ heterojunction via sol-gel route: A magnetically recyclable direct contact Z-scheme nanophotocatalyst for enhanced photocatalytic removal of ibuprofen from real sewage effluent under visible light. *Chem. Eng. J.* **2018**, *353*, 645–656. [CrossRef]
89. Wu, Y.; Meng, D.; Guo, Q.; Gao, D.; Wang, L. Study on $TiO_2$/g-$C_3N_4$ S-Scheme heterojunction photocatalyst for enhanced formaldehyde decomposition. *Opt. Mater.* **2022**, *126*, 112213. [CrossRef]
90. Talab, S.A.; Khairy, M.; Goda, M.N.; Ghoniem, M.G.; Aissa, M.A.B.; Abuhaimed, K.A.; Raza, N.; Modwi, A. Synthesis of $SnO_2$-$TiO_2$@g-$C_3N_4$ nanosorbent for the elimination of Pb (II) from synthetic wastewater. *Diam. Relat. Mater.* **2025**, *158*, 112643. [CrossRef]
91. Glažar, D.; Tomšič, B.; Jerman, I.; Chouhan, R.S.; Šuligoj, A.; Zorc, M.; Pintar, A.; Kovač, J.; Krajnc, A.; Ruiz-Zepeda, F. Surface-engineered Ag/$TiO_2$/graphitic carbon nitride nanocomposites on cotton textiles for multifunctional photocatalytic, UV shielding, and antibacterial performance. *Appl. Surf. Sci.* **2025**, *721*, 165446. [CrossRef]
92. Zhang, H.; Liu, F.; Wu, H.; Cao, X.; Sun, J.; Lei, W. In situ synthesis of g$C_3N_4$/$TiO_2$ heterostructures with enhanced photocatalytic hydrogen evolution under visible light. *RSC Adv.* **2017**, *7*, 40327–40333. [CrossRef]
93. Shahzadi, S.; Fatima, S.; ul ain, Q.; Shafiq, Z.; Janjua, M.R.S.A. A review on green synthesis of silver nanoparticles (SNPs) using plant extracts: A multifaceted approach in photocatalysis, environmental remediation, and biomedicine. *RSC Adv.* **2025**, *15*, 3858–3903. [CrossRef] [PubMed]
94. Ho, Q.D.; Lai, V.D.; Nguyen, Q.A.; Vu, D.N.; Dang, T.K.L.; La, D.D. Green synthesis of g-$C_3N_4$/$CeO_2$ nanocomposites for enhanced photocatalytic degradation of organic dye under simulated sunlight. *Diam. Relat. Mater.* **2025**, *157*, 112484. [CrossRef]
95. Khan, I.; Khan, S.; Chen, J.; Shah, S.A.; Yuan, A. Biological Inspired Green Synthesis of $TiO_2$ Coupled g-$C_3N_4$ Nanocomposites and Its Improved Activities for Sulfadiazine and Bisphenol A Degradation. *J. Clust. Sci.* **2023**, *34*, 1453–1464. [CrossRef]
96. Sofia, G.; Koventhan, C.; Kanmani, S.; Lo, A.-Y. Green synthesized rGO/$TiO_2$/g-$C_3N_4$ nanocomposites via Plectranthus amboinicus extract for efficient photocatalytic degradation of methylene blue: RSM optimization, antimicrobial and phytotoxicity assessment. *J. Environ. Chem. Eng.* **2025**, *13*, 115267. [CrossRef]
97. Ying, S.; Guan, Z.; Ofoegbu, P.C.; Clubb, P.; Rico, C.; He, F.; Hong, J. Green synthesis of nanoparticles: Current developments and limitations. *Environ. Technol. Innov.* **2022**, *26*, 102336. [CrossRef]
98. Sabzi, M.; Mousavi Anijdan, S.H.; Shamsodin, M.; Farzam, M.; Hojjati-Najafabadi, A.; Feng, P.; Park, N.; Lee, U. A Review on Sustainable Manufacturing of Ceramic-Based Thin Films by Chemical Vapor Deposition (CVD): Reactions Kinetics and the Deposition Mechanisms. *Coatings* **2023**, *13*, 188. [CrossRef]

99. Lv, S.; Ng, Y.H.; Zhu, R.; Li, S.; Wu, C.; Liu, Y.; Zhang, Y.; Jing, L.; Deng, J.; Dai, H. Phosphorus vapor assisted preparation of P-doped ultrathin hollow g-$C_3N_4$ sphere for efficient solar-to-hydrogen conversion. *Appl. Catal. B Environ.* **2021**, *297*, 120438. [CrossRef]
100. Luo, X.; Dong, Y.; Wang, D.; Duan, Y.; Lei, K.; Mao, L.; Li, Y.; Zhao, Q.; Sun, Y. Facile Synthesis of g-$C_3N_4$ Nanosheets for Effective Degradation of Organic Pollutants via Ball Milling. *Rev. Adv. Mater. Sci.* **2023**, *62*, 20230123. [CrossRef]
101. Ismael, M. One-step ultrasonic-assisted synthesis of Ni-doped g-$C_3N_4$ photocatalyst for enhanced photocatalytic hydrogen evolution. *Inorg. Chem. Commun.* **2023**, *151*, 110607. [CrossRef]
102. de Conti, M.C.M.D.; Dey, S.; Pottker, W.E.; La Porta, F.A. An overview into advantages and applications of conventional and unconventional hydro(solvo)thermal approaches for novel advanced materials design. *Mater. Today Sustain.* **2023**, *23*, 100458. [CrossRef]
103. Tazim, T.Q.; Kawsar, M.; Sahadat Hossain, M.; Bahadur, N.M.; Ahmed, S. Hydrothermal synthesis of nano-metal oxides for structural modification: A review. *Next Nanotechnol.* **2025**, *7*, 100167. [CrossRef]
104. Li, S.; Ma, H.; Ouyang, P.; Li, Y.; Duan, Y.; Zhou, Y.; Ong, W.-J.; Dong, F. Advanced microwave synthesis strategies for innovative photocatalyst design. *Green Energy Environ.* **2025**, *10*, 1597–1623. [CrossRef]
105. Saman, F.; Se Ling, C.H.; Ayub, A.; Rafeny, N.H.B.; Mahadi, A.H.; Subagyo, R.; Nugraha, R.E.; Prasetyoko, D.; Bahruji, H. Review on synthesis and modification of g-$C_3N_4$ for photocatalytic $H_2$ production. *Int. J. Hydrogen Energy* **2024**, *77*, 1090–1116. [CrossRef]
106. Innocenzi, P. Sol-gel processing for advanced ceramics, a perspective. *Open Ceram.* **2023**, *16*, 100477. [CrossRef]
107. Nassar, K.I.; Teixeira, S.S.; Graça, M.P.F. Sol–Gel-Synthesized Metal Oxide Nanostructures: Advancements and Prospects for Spintronic Applications—A Comprehensive Review. *Gels* **2025**, *11*, 657. [CrossRef] [PubMed]
108. Gupta, D.; Boora, A.; Thakur, A.; Gupta, T.K. Green and sustainable synthesis of nanomaterials: Recent advancements and limitations. *Environ. Res.* **2023**, *231*, 116316. [CrossRef] [PubMed]
109. Huang, L.; Liu, H.; Zhang, T.C.; Wang, Y.; Yuan, S. Peroxymonosulfate-assisted $BiVO_4$/exfoliated g-$C_3N_4$ heterojunction for high-performance photodegradation of tetracycline induced by visible light. *Ind. Eng. Chem. Res.* **2022**, *61*, 16418–16430. [CrossRef]
110. Wang, Z.; Liang, L.; Li, N.; Wu, S.; Cheng, Z.; Yan, B.; Chen, G. Peroxymonosulfate Activation by Bi-Fe Oxide Co-Doped Graphitic Carbon Nitride for Degradation of Sulfamethoxazole: Performance and Mechanism. *Appl. Sci.* **2024**, *14*, 3181. [CrossRef]
111. Dou, L.; Huang, W.; Huang, Y.; Wang, Y.; Chen, Y.; Li, J.; Gao, X.; Li, N.; Lai, B. Carbon-rich g-$C_3N_4$ nanotubes with highly dispersed cobalt as a catalyst to degrade sulfamethoxazole in the Vis-PMS system: Nonradical oxidation role. *Ind. Eng. Chem. Res.* **2024**, *63*, 5697–5709. [CrossRef]
112. Wu, G.; Cai, Z.; Li, G.; Tai, G.; Huang, X.; Zhu, L.; Zhao, Z.; Pan, Y.; Xing, W. In situ construction of the van Der Waals heterojunction based on $Co_3O_4$/g-$C_3N_4$ for the highly efficient degradation of tetracycline under visible light. *Langmuir* **2025**, *41*, 12127–12139. [CrossRef] [PubMed]
113. Zhong, X.; Ji, M.; Wu, W.; Lu, C.; Liu, W.; Jiang, F. Enhanced Degradation of Levofloxacin through Visible-Light-Driven Peroxymonosulfate Activation over $CuInS_2$/g-$C_3N_4$ Heterojunctions. *Nanomaterials* **2024**, *14*, 74. [CrossRef] [PubMed]
114. Wang, Z.; Yin, E.; Yin, Y.; Du, B.; Jiang, R.; Xu, L.; Li, X. Co/g-$C_3N_4$ photocatalysts as an efficient mediator to activate peroxymonosulfate under visible light for degrading ciprofloxacin: Characterization, intermediates and mechanism. *J. Environ. Chem. Eng.* **2025**, *13*, 116595. [CrossRef]
115. Shi, Y.; Li, J.; Wan, D.; Huang, J.; Liu, Y. Peroxymonosulfate-enhanced photocatalysis by carbonyl-modified g-$C_3N_4$ for effective degradation of the tetracycline hydrochloride. *Sci. Total Environ.* **2020**, *749*, 142313. [CrossRef] [PubMed]
116. Zhang, W.; Liu, H.; Chen, Z.; Yang, Z.; Zhang, X.; Wang, X. In Situ Construction of CdS/g-$C_3N_4$ Heterojunctions in Spent Thiolation@Wood-Aerogel for Efficient Excitation Peroxymonosulfate to Degradation Tetracycline. *ACS Appl. Mater. Interfaces* **2024**, *16*, 28353–28366. [CrossRef] [PubMed]
117. Lu, G.; Li, X.; Lu, P.; Guo, H.; Wang, Z.; Zhang, Q.; Li, Y.; Sun, W.; An, J.; Zhang, Z. Z-Type Heterojunction $MnO_2$@g-$C_3N_4$ Photocatalyst-Activated Peroxymonosulfate for the Removal of Tetracycline Hydrochloride in Water. *Toxics* **2024**, *12*, 70. [CrossRef] [PubMed]
118. Mo, C.; Zhou, L.; Zheng, J.; Liang, B.; Huang, H.; Huang, G.; Liang, J.; Li, S.; Junaid, M.; Wang, J.; et al. Efficient photodegradation of antibiotics by g-$C_3N_4$ and 3D flower-like $Bi_2WO_6$ perovskite structure: Insights into the preparation, evaluation, and potential mechanism. *Chemosphere* **2024**, *359*, 142286. [CrossRef] [PubMed]
119. Wang, Q.; Li, Y.; Huang, F.; Song, S.; Ai, G.; Xin, X.; Zhao, B.; Zheng, Y.; Zhang, Z. Recent Advances in g-$C_3N_4$-Based Materials and Their Application in Energy and Environmental Sustainability. *Molecules* **2023**, *28*, 432. [CrossRef] [PubMed]
120. Guo, P.; Hu, X. Co, Fe co-doped g-$C_3N_4$ composites as peroxymonosulfate activators under visible light irradiation for levofloxacin degradation: Characterization, performance and synergy mechanism. *Colloids Surf. A Physicochem. Eng. Asp.* **2022**, *648*, 129423. [CrossRef]
121. Bai, Y.; Dong, W.; Zhang, Q.; She, H.; Chen, X.; Wang, Q. Preparation of FeCu-LDH/g-$C_3N_4$ catalysts and synergistic activation of potassium persulfate for photocatalytic significant degradation of tetracycline. *J. Alloys Compd.* **2025**, *1033*, 181237. [CrossRef]

122. Lu, Y.; Fu, M.; Cheng, C.; Yang, H.; Ni, X.; Guo, J.; Cao, S. High-efficiency and stable Z-scheme heterojunction of $Co_9S_8$ anchored by g-$C_3N_4$ for peroxymonosulfate activation. *J. Environ. Chem. Eng.* **2024**, *12*, 114524. [CrossRef]
123. Tang, R.; Gong, D.; Deng, Y.; Xiong, S.; Zheng, J.; Li, L.; Zhou, Z.; Su, L.; Zhao, J. π-π stacking derived from graphene-like biochar/g-$C_3N_4$ with tunable band structure for photocatalytic antibiotics degradation via peroxymonosulfate activation. *J. Hazard. Mater.* **2022**, *423*, 126944. [CrossRef] [PubMed]
124. Nguyen, T.G.; Nguyen, M.D.; Do, T.L.; Dang, V.T.; Hoang, V.H.; Nguyen, T.H. Synergistic doping of B/Mn in tubular g-$C_3N_4$ for enhanced photodegradation of tetracycline using peroxymonosulfate. *Mater. Res. Express* **2025**, *12*, 055004. [CrossRef]
125. Xiao, Q.; Nan, J. Cu–Co–O-Codoped Graphite Carbon Nitride as an Efficient Peroxymonosulfate Activator for Sulfamethoxazole Degradation: Characterization, Performance, and Mechanism. *Water* **2025**, *17*, 2161. [CrossRef]
126. Hong, J.; Dong, J.; Zhang, X.; Liu, G.; Li, L.; Wang, B.; Ji, M.; Li, H.; Xia, J. The synergistic effect of low concentration of peroxymonosulfate and visible light photocatalysis over FeOOH quantum dots/hollow g-$C_3N_4$ nanotubes S-scheme heterojunction for effectively antibiotics degradation. *J. Environ. Chem. Eng.* **2025**, *13*, 115777. [CrossRef]
127. Shi, H.; He, Y.; Li, Y.; Luo, P. Unraveling the synergy mechanism between photocatalysis and peroxymonosulfate activation on a Co/Fe bimetal-doped carbon nitride. *ACS Catal.* **2023**, *13*, 8973–8986. [CrossRef]
128. Fang, H.; Gao, J.; Wang, J.; Xu, J.; Wang, L. Oxygen-doped and pyridine-grafted g-$C_3N_4$ for visible-light driven peroxymonosulfate activation: Insights of enhanced tetracycline degradation mechanism. *Sep. Purif. Technol.* **2023**, *314*, 123565. [CrossRef]
129. Le, M.-V.; Nguyen, Q.-T.-N.; Huynh, N.-D.-T.; Pham, N.-D.; Truong, C.-H.; Tran, H.-T.; Le, P.-N.-M.; Ngo, T.-H.; Huynh, H.T. Direct Z-scheme $CoTiO_3$/g-$C_3N_4$ nanoparticles: Fabrication and application as a photocatalyst for degradation of tetracycline hydrochloride assisted by peroxydisulfate or peroxymonosulfate under simulated sunlight. *Nanotechnol. Environ. Eng.* **2023**, *8*, 675–690. [CrossRef]
130. Zhang, X.; Tian, Y.; Zhou, L.; Wang, L.; Zhang, J.; Liu, Y.; Lei, J. Efficient degradation of levofloxacin using a g-$C_3N_4$@glucose-derived carbon catalyst with adjustable N content via peroxymonosulfate activation. *Chemosphere* **2023**, *314*, 137684. [CrossRef] [PubMed]
131. Cao, G.; Shen, Z.; Cui, J.; Yu, M.; Li, W. Bifunctional activation of peroxymonosulfate over CuS/g-$C_3N_4$ composite for efficient degradation of tetracycline antibiotics. *Chem. Eng. J.* **2024**, *483*, 149082. [CrossRef]
132. Alotaibi, M.A.; Alharthi, A.I.; Ahmed, A.; Khalid, A. Highly efficient degradation of moxifloxacin through heterogeneous activation of peroxymonosulfate using $Co_3O_4$-g-$C_3N_4$ composites: Optimization of interfering factors. *Surf. Interfaces.* **2024**, *52*, 104788. [CrossRef]
133. Yang, H.; Cao, X.; He, Y.; Zhang, X.; Zhang, P.; Wang, X.; Liu, Y.; Xu, S.; Fang, Y.; Gu, L. Fe, N-CQDs triggered the fabrication of alginate encapsulated g-$C_3N_4$ hydrogel for efficient photocatalytic activation of PMS and antibiotic degradation. *Carbohydr. Polym.* **2025**, *351*, 123072. [CrossRef] [PubMed]
134. Guo, P.; Ding, L.; Hu, X. Enhanced degradation of levofloxacin using photocatalysis and peroxymonosulfate oxidation processes by Z-scheme $BiVO_4$/g-$C_3N_4$ heterojunction. *J. Alloys Compd.* **2025**, *1010*, 177886. [CrossRef]
135. Zhang, P.; Cao, X.; Gu, L.; Yu, H.; Wu, F.; Liu, Y.; Liu, X.; Gao, Y.; Zhang, H. Embedded iron and nitrogen co-doped carbon quantum dots within g-$C_3N_4$ as an exceptional PMS photocatalytic activator for sulfamethoxazole degradation: The key role of FeN bridge. *Sep. Purif. Technol.* **2024**, *342*, 126975. [CrossRef]
136. Peng, Y.; Shang, J.; Xie, J.; Jiang, X.; Li, R.; Hu, X.; Huang, Y.; Lu, P. Visible-light-driven activation of peroxymonosulfate by g-$C_3N_4$/$CeO_2$ heterojunction for efficient tetracycline degradation. *Chem. Phys. Lett.* **2026**, *893*, 142819. [CrossRef]
137. Aali, R.; Azari, H.; Pasalari, H.; Yaghmaeian, K.; Yousefi, M.; Azari, A.; Yari, A.R.; Sharifi, N.; Kamani, H.; Dowlati, M. Enhanced sulfadiazine degradation through synergistic visible light assisted peroxymonosulfate activation using a magnetic $Fe_3O_4$-$ZnIn_2S_4$ catalyst. *Sci. Rep.* **2025**, *15*, 25013. [CrossRef] [PubMed]
138. Li, S.; Tang, Y.; Wang, M.; Kang, J.; Jin, C.; Liu, J.; Li, Z.; Zhu, J. NiO/g-$C_3N_4$ 2D/2D heterojunction catalyst as efficient peroxymonosulfate activators toward tetracycline degradation: Characterization, performance and mechanism. *J. Alloys Compd.* **2021**, *880*, 160547. [CrossRef]
139. Mu, Z.; Chen, H.; Feng, X.; Xie, T.; Wang, D.; Lin, Y. Improved photocatalytic activation of PMS using Co-doped g-$C_3N_4$ composites for effective degradation of tetracycline: Catalyst performance, photogenerated carrier transfer and degradation mechanism. *Mater. Res. Bull.* **2025**, *182*, 113132. [CrossRef]
140. Ruiz-Santoyo, V.; Cabrera-Germán, D.; Garcia-Carvajal, S.; Arenas-Arrocena, M.C. In Situ Hydrothermal Synthesis of a g-$C_3N_4$–$Bi_2O_3$ Heterojunction for Efficient Photocatalytic Degradation of Tetracycline Hydrochloride. *Top. Catal.* **2025**. [CrossRef]
141. Ahmad, W.; Akhtar, N.; Choi, A.; Ateeq, M.; Shah, N.S.; Khan, J.A.; Al-Anazi, A.; Han, C. Hydrothermally engineered $TiO_2$/CdS nanocomposite for efficient photocatalytic degradation of carbamazepine, hydrogen evolution and antibacterial applications. *Sep. Purif. Technol.* **2026**, *383*, 136131. [CrossRef]
142. Reza, K.M.; Kurny, A.S.W.; Gulshan, F. Parameters affecting the photocatalytic degradation of dyes using $TiO_2$: A review. *Appl. Water Sci.* **2017**, *7*, 1569–1578. [CrossRef]

143. Zyoud, A.; Zyoud, A.H.; Zyoud, S.H.; Nassar, H.; Zyoud, S.H.; Qamhieh, N.; Hajamohideen, A.; Hilal, H.S. Photocatalytic degradation of aqueous methylene blue using ca-alginate supported ZnO nanoparticles: Point of zero charge role in adsorption and photodegradation. *Environ. Sci. Pollut. Res.* **2023**, *30*, 68435–68449. [CrossRef] [PubMed]
144. Lee, D.-E.; Kim, M.-K.; Danish, M.; Jo, W.-K. State-of-the-art review on photocatalysis for efficient wastewater treatment: Attractive approach in photocatalyst design and parameters affecting the photocatalytic degradation. *Catal. Commun.* **2023**, *183*, 106764. [CrossRef]
145. Wang, L.; Cheng, W.; Yang, X.; Wang, R.; Liu, R.; Zhu, Y.; Yi, Y.; Tang, Y.; Wang, Z. An atomic insight into reaction pathways and temperature effects in the degradation of polyethylene, polypropylene and polystyrene. *Polym. Degrad. Stab.* **2023**, *215*, 110450. [CrossRef]
146. Rafiq, A.; Ikram, M.; Ali, S.; Niaz, F.; Khan, M.; Khan, Q.; Maqbool, M. Photocatalytic degradation of dyes using semiconductor photocatalysts to clean industrial water pollution. *J. Ind. Eng. Chem.* **2021**, *97*, 111–128. [CrossRef]
147. Anwar, M.; Shah, S.I.A.; Hussain, I.; Ahmad, W.; Shah, N.S.; Al-Anazi, A.; Khan, J.A. Synthesis of nitrogen-doped graphene oxide for photocatalytic degradation of atrazine: Kinetics and mechanism. *Diam. Relat. Mater.* **2026**, *162*, 113201. [CrossRef]
148. Gao, S.; Chen, X.; Fang, X.; Cheng, Z.; Wang, Y.; Gao, D.; Guo, Q.; Wang, L.; Hu, X. Photocatalytic degradation of tetracycline by g-$C_3N_4$/stilbite under visible light: Mechanistic insights and degradation pathways. *Mater. Res. Bull.* **2024**, *180*, 113008. [CrossRef]
149. Kundu, S.; Pal, A.; Dikshit, A.K. UV induced degradation of herbicide 2,4-D: Kinetics, mechanism and effect of various conditions on the degradation. *Sep. Purif. Technol.* **2005**, *44*, 121–129. [CrossRef]

**Disclaimer/Publisher's Note:** The statements, opinions and data contained in all publications are solely those of the individual author(s) and contributor(s) and not of MDPI and/or the editor(s). MDPI and/or the editor(s) disclaim responsibility for any injury to people or property resulting from any ideas, methods, instructions or products referred to in the content.